Search for Unstable Neutral and Charged Heavy Leptons in e^+e^- Collisions at $\sqrt{s} = 161$ GeV

The OPAL Collaboration

Abstract

Searches for unstable neutral and charged heavy leptons (L^0, $L^\pm$) have been performed using a data sample of 3.12 pb^{-1} at a centre-of-mass energy of $\sqrt{s} \approx 161$ GeV collected with the OPAL detector at LEP during July 1996. No candidates event were observed, and so preliminary lower limits have been derived on heavy lepton masses in different models. If an unstable Dirac neutral heavy lepton L^0 decays only into eW^*, μW^* or τW^*, the lower limits on its mass at 95% C.L. are 64.5 GeV, 64.6 GeV and 60.8 GeV, respectively. The limits are modified for a Majorana L^0 to 54.5 GeV, 55.3 GeV and 50.1 GeV, respectively. For charged heavy leptons, a lower mass limit of 67.5 GeV at 95% C.L. was obtained, if $L^\pm$ decays into a stable heavy neutrino ν_L and $W^{*\pm}$, and if $m_{L^\pm} - m_{\nu_L} > 10$ GeV. If $L^\pm$ decays through lepton flavour mixing into a massless neutrino ν_ℓ and $W^{*\pm}$, the lower limit on $m_{L^\pm}$ was determined to be 66.0 GeV at 95% C.L.

1 Introduction

This paper presents searches for pair production of unstable neutral heavy leptons $L^0\bar{L}^0$ and unstable charged heavy leptons L^+L^- in e^+e^- collisions[1]. The data used in this analysis correspond to an integrated luminosity of 3.12 pb^{-1} at a centre-of-mass energy of $\sqrt{s} \approx 161$ GeV collected with the OPAL detector at LEP during July 1996.

The precise measurements of the Z boson parameters by the LEP and SLC experiments have determined the number of species of light neutrinos to be three [1]. However, this does not exclude a fourth generation in which all the fermions are heavy. The lower mass limit based on LEP running around the Z^0 peak (LEP1) for the fourth generation stable neutrino (ν_L) was 45.0 GeV for a Dirac neutrino and 39.5 GeV for a Majorana neutrino [1]. The cross-sections for the $e^+e^- \rightarrow L^0\bar{L}^0$ and $e^+e^- \rightarrow L^+L^-$ processes are given in Ref. [2]. The cross-sections for $L^0\bar{L}^0$ and L^+L^- productions at a centre-of-mass energy of $\sqrt{s} = 161$ GeV are plotted in Fig. 1.

Neutral heavy lepton pairs $L^0\bar{L}^0$ could be produced in e^+e^- annihilation via a virtual Z boson. The following decay mode was considered:

(A) $L^0 \rightarrow \ell W^*$ via lepton flavour mixing, where ℓ is e, μ or τ, and W^* is a virtual W boson.

The Majorana L^0 can decay into either $\ell^- W^{*+}$ or $\ell^+ W^{*-}$. Therefore the charge correlation between the two light leptons was not used in the analysis, in order to be sensitive to both Dirac and Majorana L^0. The lower mass limit at $\sqrt{s} = 130$ and 136 GeV (LEP1.5) at LEP for an unstable L^0 was 63.0 GeV for a Dirac L^0 and 54.3 GeV for a Majorana L^0, if the coupling $L^0L^0Z^*$ is the same as for $\nu_\ell\nu_\ell Z^*$ [1, 3, 4]. The visible energy of these events is expected to be large and there should be at least four charged particles, including at least two light leptons (e, μ or τ), in an event.

Charged heavy lepton pairs L^+L^- could be produced in e^+e^- annihilation via a virtual Z^0 boson or a virtual photon. The ordinary V–A coupling was assumed for the $L^-\nu_L W^{*-}$ and $L^-\nu_\ell W^{*-}$ vertices. The following two cases were studied:

(B) $L^- \rightarrow \nu_L W^{*-}$, where ν_L is a stable heavy neutrino and assumed to be heavier than the lower mass limit from the LEP experiments [1, 3].

(C) $L^- \rightarrow \nu_\ell W^{*-}$, where ν_ℓ is ν_e, ν_μ or ν_τ. The decay occurs via lepton flavour mixing. The experimental limit from LEP data was $m_{L^-} > 65.0$ GeV [1, 3, 4].

The expected experimental signature for L^+L^- events for both cases is that of a multijet[2] event with a large, unbalanced transverse momentum with respect to the beam axis. If all the visible decay products of L^- and L^+ happened to be in the same hemisphere, the event topology could be a monojet. The events in case (B) are expected to have a smaller visible energy than for case (C), because the two heavy neutrinos carry away more energy and momentum.

In this paper, L^0 and L^- were assumed to be unstable. Cascade decays ($L^0 \rightarrow L^- \rightarrow \nu_\ell$, $L^- \rightarrow L^0 \rightarrow \ell$) of heavy leptons were not considered in this analysis. The analysis was

---

[1]Throughout this paper, charge conjugation is implicitly assumed. L^- denotes an unstable charged heavy lepton, L^0 denotes an unstable neutral heavy lepton and ν_L denotes a stable heavy neutrino.

[2]An isolated lepton is treated as a jet.

designed to have a good sensitivity for heavy leptons with a decay length shorter than about a few cm. Namely, the mixing parameters of L^0–ν_ℓ and L^-–ℓ^- were assumed to satisfy the condition $\sum_\ell |V_{L^0\ell}|^2 > \mathcal{O}(10^{-11})$ for case (A), and $\sum_\ell |V_{L^-\nu_\ell}|^2 > \mathcal{O}(10^{-11})$ for case (C), where $V_{L^0\ell}$ is the flavour mixing parameter between a neutral heavy lepton and a light lepton (e, μ or τ) and $V_{L^-\nu_\ell}$ is the flavour mixing parameter between a charged heavy lepton and a light neutrino (ν_e, ν_μ or ν_τ).

The two W^* bosons in an $L^0\bar{L}^0$ or L^+L^- event can decay either leptonically or hadronically. The analysis presented here is sensitive to all the possible combinations of the decay topologies and was designed to search for heavy leptons with masses above the LEP experimental limits.

2 The OPAL Detector and Event Simulation

2.1 The OPAL Detector

The OPAL detector, which is described in detail in [5], is a multipurpose apparatus having nearly complete solid angle coverage. The central detector consists of a system of tracking chambers providing charged particle tracking over 96% of the full solid angle[3] inside a uniform 0.435 T magnetic field. The solenoid is surrounded by a time-of-flight (TOF) scintillating counter array. A lead-glass electromagnetic (EM) calorimeter located outside the magnet coil covers the full azimuthal range with excellent hermeticity in the polar angle range of $|\cos\theta| < 0.82$ for the barrel region and $0.81 < |\cos\theta| < 0.984$ for the endcap region. The magnet return yoke is instrumented for hadron calorimetry (HCAL), consisting of barrel and endcap sections along with pole tips detectors that together cover the region $|\cos\theta| < 0.99$. Calorimeters close to the beam axis measure the luminosity using small angle Bhabha scattering events and complete the geometrical acceptance down to 26 mrad from the beam axis. These include the forward detectors which are lead-scintillator sandwich calorimeters and, at smaller angles, silicon tungsten calorimeters (SW) [6] located on both sides of the interaction point. The gap between the endcap EM calorimeter and the forward detector is filled by an additional lead-scintillator electromagnetic calorimeter, called the gamma-catcher.

2.2 Monte Carlo Event Simulation

$L^0\bar{L}^0$ and L^+L^- events have been generated using the TIPTOP [7] generator, which includes the effects of spin correlations in the weak decays. The generator was modified so that JET-SET 7.4 [8] could be used for the hadronization, which includes gluon radiation. Initial state photon radiation was implemented in the generator based on the calculations of Berends and Kleiss [9]. $L^0\bar{L}^0$ events were generated at 7 values of heavy neutral lepton mass from 50 to 80 GeV for the three different final states $eW^* + eW^*$, $\mu W^* + \mu W^*$ and $\tau W^* + \tau W^*$. L^+L^- events were generated at 26 points in the (m_{L^-}, m_{ν_L}) plane for case (B) and at 5 mass values of heavy leptons from 60 to 80 GeV for case (C).

The following background processes were simulated in this analysis:

- Hadronic events with an isolated lepton coming from a heavy flavour decay, or with an

---

[3]A right-handed coordinate system is adopted, where the x-axis points to the centre of the LEP ring, and positive z is along the electron beam direction. The angles θ and ϕ are the polar and azimuthal angles, respectively.

isolated track misidentified as a lepton, are an important background for the L^0 search. In the L^- search, the dominant $q\bar{q}(\gamma)$ background events are multijet events with one or more poorly reconstructed jet momenta. The PYTHIA 5.7 [10] Monte Carlo generator was used for multihadron events.

- The KORALZ [11] event generator was used for the generation of $\tau^+\tau^-(\gamma)$ and $\mu^+\mu^-(\gamma)$ events. A sample of $e^+e^-(\gamma)$ events was generated using the BHWIDE generator [12]. Radiative and non-radiative τ pairs are a potential source of background for the topology of two acoplanar jets, because neutrinos from the τ decays carry away energy and momentum.

- In case (B), particularly for a small mass difference between L^- and $\nu_{\rm L}$, events from two-photon processes are the main background. Since the visible energy is small in this case, the two-photon event topology is similar to the signal event topology. The PYTHIA 5.7 and PHO-JET [13] Monte Carlo generators were used for generating events from two-photon processes where the Q^2 of both photons is smaller than 1.0 GeV^2 and the invariant mass of the photon-photon system ($M^2_{\gamma\gamma}$) is greater than 4 GeV^2. For events with higher Q^2 the generators PYTHIA 5.7 and HERWIG [14] were used. Four lepton events were generated by VERMASEREN [15]. Event samples for all the possible processes (final state hadrons from point-like $\gamma\gamma \rightarrow q\bar{q}$ processes and from vector meson dominance, and all $e^+e^-\ell^+\ell^-$ final states) were generated. Two-photon events were not generated in the region $Q^2 < 1.0$ GeV^2 and $M^2_{\gamma\gamma} < 4$ GeV^2, or $Q^2 > 1.0$ GeV^2 and $M^2_{\gamma\gamma} < 3$ GeV^2. This region did not represent a serious background to the search presented here.

- Events from four-fermion processes ($\ell^+\ell^-q\bar{q}$, $\ell\nu_\ell q\bar{q}'$, $\nu_\ell\bar{\nu}_\ell q\bar{q}$, $\nu_\ell\nu_\ell\ell^+\ell^-$), including W^+W^- events, are a serious background for the $L^0\bar{L}^0$ and L^+L^- searches. The EXCALIBUR [16] generator was used to generate all four-fermion processes and W^+W^- events. Since the event sample that we have generated using the EXCALIBUR Monte Carlo generator does not include $e^+e^- \rightarrow We\nu$ and $e^+e^- \rightarrow Z^*/\gamma^*e^+e^-$ events in which one of the electrons scatters at a very low angle, these events were generated using the PYTHIA generator.

Generated signal and background events were processed through the full simulation of the OPAL detector [17], and the same event analysis chain was applied to these simulated events as to the data.

3 Data Analysis

Charged particle tracks were selected with the same track quality requirements as in Ref. [18, 19]. Tracks were required to have at least 20 measured spatial hits, more than 50% of the hits geometrically expected, and a transverse momentum exceeding 100 MeV. Electromagnetic clusters in the barrel region were required to have an energy of at least 100 MeV, and the clusters in the endcaps to have an energy of at least 250 MeV and to contain at least two adjacent lead glass blocks. Clusters in the hadron calorimeters were required to have an energy of at least 0.6 GeV in the barrel and endcaps, and at least 2 GeV in the pole tips detectors. The SW clusters were required to have at least 2 GeV of deposited energy. Furthermore the clusters were required to have at least 1.5 GeV in each forward calorimeters and 5 GeV in the gamma-catcher. Background from cosmic rays was suppressed by requiring at least one track to have a hit in the TOF counter within 10 ns of the expected time-of-flight.

Event observables such as the total visible energy or hemisphere momenta were calculated as follows. The track momenta and the momentum vectors of EM or HCAL calorimeter clusters

not associated with charged tracks were first summed. When a calorimeter cluster was associated to charged tracks, the scalar sum of the associated charged track momenta was subtracted from the cluster energy before including the cluster, to reduce double counting. If the energy of a cluster was smaller than the scalar sum of the associated track momenta, the cluster energy was not used. The masses of all charged particles were set to the charged pion mass and the invariant masses of the energy clusters were assumed to be zero. Jets were formed using the Durham algorithm [20] with a jet resolution parameter of $y_{cut} = 0.004$.

3.1 Selection of $L^0\bar{L}^0$ candidates (case A)

The following event selection criteria were applied. The numbers of remaining events up to and including each cut are listed in Table 1, for data and for simulated background and signal samples.

(A1) The number of tracks was required to be at least four, and the ratio of the number of tracks which satisfied the selection criteria to the total number of reconstructed tracks was required to be larger than 0.2 in order to reject beam-gas and beam-wall backgrounds.

(A2) In order to reduce the background from two-photon processes and multihadronic events in which one of the jet axes was close to the beam direction, the total energy deposited in each silicon tungsten calorimeter was required to be less than 5 GeV. Furthermore the energy was required to be less than 2 GeV in each forward calorimeter and less than 5 GeV in each side of the gamma-catcher.

(A3) The cosine of the polar angle of the thrust axis ($|\cos\theta_{\text{thrust}}|$) was required to be less than 0.95 in order to reduce beam-gas and beam-wall background events as well as events from two-photon processes.

(A4) The visible energy was required to be greater than $0.45\sqrt{s}$ to reduce background from two-photon processes. The visible energy distributions of the data with the simulated background events and the expected signal events before this cut are plotted in Fig. 2a and Fig. 2b, respectively. The visible energy distribution of the data agrees very well with the Monte Carlo prediction in Fig. 2a.

(A5) If the missing energy was larger than 30 GeV, the polar angle of the missing momentum direction θ_{miss} was required to satisfy $|\cos\theta_{\text{miss}}| < 0.95$. One of the final states for the expected signals is $\ell\ell qq'q''q'''$ which has full visible energy. In this case the missing momentum direction is not meaningful, and hence a missing energy threshold is applied. With this cut "radiative return" events from $e^+e^- \to Z\gamma$ were reduced, because this background events have a large missing energy and have a peak at $|\cos\theta_{\text{miss}}| = 1.0$ on the $|\cos\theta_{\text{miss}}|$ distributions.

(A6) The number of jets was required to be greater than or equal to four. With this requirement a large fraction of the multihadron background was removed. The distributions of the number of jets after cut (A5) are shown in Fig. 3a for the data and the simulated background events, and in Fig. 3b for the simulated $L^0\bar{L}^0$ events.

(A7) The number of isolated leptons (e, μ or τ) was required to be at least two. The selection criteria for isolated leptons are listed below.

The momentum of an electron or muon candidate was required to be less than 40 GeV and larger than 2 GeV. Electrons were selected using the artificial neural network described in [21]. Muons were identified as the central detector track which gave the best match to a

case (A)	data	total bkg.	$q\bar{q}(\gamma)$	$\ell\ell(\gamma)$	'$\gamma\gamma$'	4-f	$L^0\bar{L}^0$		
m_{L^0} (GeV) Decay mode							65 tau	70 muon	70 electron
no cuts	–	–	459.5	2630	67686	62.0	1000	1000	1000
cut (A1)	17.8k	15.5k	446.1	28.4	15.1k	20.8	983	986	980
cut (A2)	10.1k	8958	332.5	25.5	8584	16.3	892	911	880
cut (A3)	6201	5317	321.6	24.8	4955	15.7	848	871	834
cut (A4)	333	361.0	320.4	23.1	2.38	15.1	822	868	832
cut (A5)	187	197.6	163.9	19.9	0.41	13.4	788	831	814
cut (A6)	33	34.3	27.5	0.09	0.05	6.61	693	767	756
cut (A7)	1	0.40	0.09	0.02	0.00	0.29	278	545	498
cut (A8)	0	0.21	0.05	0.01	0.00	0.15	268	479	446

Table 1: *The numbers of events remaining (in the $L^0\bar{L}^0$ search), normalised to the integrated luminosity are compared with the data (corresponding to 3.12 pb^{-1}) after each cut for various background processes. Numbers are also given for three samples of simulated $L^0\bar{L}^0$ events (starting from 1000 events in each sample). The numbers of events expected from two-photon processes ('$\gamma\gamma$') do not include the region $M_{\gamma\gamma}^2 < 4$ GeV^2 with $Q^2 < 1.0$ GeV^2, which explains the difference between data and Monte Carlo before cut (A4).*

muon chamber track segment [22]. In the region not covered by the muon chambers, muons were identified using the hadron calorimeters as described in [23]. No additional tracks were allowed within a cone with a half-angle of 15° around an electron or muon track.

The reconstructed jets described above were used to identify taus. A jet was identified as a one-prong tau decay if the following four conditions were satisfied: (1) the jet contained a track with momentum larger than 3 GeV and less than 30 GeV, (2) the momenta of all the other tracks in the same jet were less than 1 GeV, (3) no other track was found within a cone of half-angle 15° around the high momentum track, and (4) the invariant mass calculated from the track and all cluster momenta within the cone was less than 2.5 GeV. The loose invariant mass cut was applied in order to retain τ candidates which were close to other jets. A jet was identified as a three-prong tau decay if the following three criteria were satisfied: (1) there were only three tracks in the jet and all three tracks were inside a cone with a half-angle of 15° around the jet axis, (2) the vector sum of the three charged particle momenta had magnitude greater than 3 GeV, and (3) the invariant mass of all tracks and clusters within the cone was less than 2.5 GeV.

The distributions of the number of isolated leptons after cut (A6) are plotted in Fig. 3c for the data and the simulated background events, and in Fig. 3d for the simulated $L^0\bar{L}^0$ events.

(A8) Fig. 4 shows distributions of the numbers of jets and visible energy normalized to centre-of-mass energy after cut (A7). The visible energy was required to be smaller than $0.85\sqrt{s}$ if the number of reconstructed jets was four. Since the 5 jet and 6 jet events are rather rare in the background but $L^0\bar{L}^0 \rightarrow \ell^-W^{*+}\ell^+W^{*-} \rightarrow \ell\ell\ell\nu_\ell qq'$ or $\ell\ell\, qq'q''q'''$ events have naturally 5 or 6 jets, we accepted all events with at least 5 jets. In the 4 jet case the four-fermion process $\ell\ell qq$ is a severe background. If in this process ℓ is an e or μ, the events should have a small missing energy. On the other hand the signal events from $L^0\bar{L}^0 \rightarrow \ell^-W^{*+}\ell^+W^{*-} \rightarrow \ell\ell\ell\nu_\ell\ell\nu_\ell$ are

naturally 4 jet events with a large missing energy. The four-fermion background can therefore be reduced by appling the visible energy cut.

Decay	m_{L^0}=50 GeV	55 GeV	60 GeV	65 GeV	70 GeV	75 GeV
$L^0 \to eW^*$	35.3 ± 1.5	35.2 ± 1.5	37.7 ± 1.5	42.5 ± 1.6	44.6 ± 1.6	44.5 ± 1.6
$L^0 \to \mu W^*$	39.0 ± 1.5	42.3 ± 1.6	39.8 ± 1.5	43.2 ± 1.6	47.9 ± 1.6	47.5 ± 1.6
$L^0 \to \tau W^*$	25.8 ± 1.4	28.1 ± 1.4	27.9 ± 1.4	26.8 ± 1.4	29.8 ± 1.4	27.3 ± 1.4

Table 2: *The selection efficiencies (in %) of L^0 candidates for three decay modes ($L^0 \to eW^*$, μW^* and τW^*) as a function of m_{L^0}. The errors are statistical only.*

No event was observed in the data after the above selection. This result was consistent with the number of expected background events of 0.21. The detection efficiencies for $L^0 \bar{L}^0$ events are summarized in table 2.

These analysis criteria are sensitive to all light leptons (e, μ and τ). The three different final states of $L^0\bar{L}^0 \to eW^* + eW^*$, $\mu W^* + \mu W^*$ and $\tau W^* + \tau W^*$ were considered in calculating the efficiencies. The mixed decay products of $L^0\bar{L}^0$ ($L^0\bar{L}^0 \to eW^*\mu W^*$, $eW^*\tau W^*$ or $\mu W^*\tau W^*$) are not taken into account. The efficiencies would have values intermediate to the unmixed case.

3.2   Selection of $L^+L^- \to \nu_L W^{*+}\nu_L W^{*-}$ candidates (case B)

The number of events remaining after each cut are listed in Table 3 for case (B). For comparison the table also includes the corresponding numbers of simulated background and L^+L^- events.

The following selection criteria were applied:
(B1) The number of charged tracks was required to be at least two, and the ratio of the number of tracks which satisfied the selection criteria to the total number of reconstructed tracks was required to be greater than 0.2.

(B2) The criteria for energy deposits in the silicon tungsten calorimeter, the forward calorimeter and the gamma-catcher were identical to those in the $L^0\bar{L}^0$ analysis.

(B3) The cosine of the polar angle of the thrust axis ($|\cos\theta_{thrust}|$) was required to be less than 0.9. The $|\cos\theta_{thrust}|$ cut is harder than in the L^0 analysis because the acoplanarity angle, which is discussed later, becomes unreliable if the jet axes are close to the beam direction.

(B4) Events from two-photon processes with a small visible energy were efficiently reduced by demanding the event transverse momentum (P_t) calculated excluding the hadron calorimeter clusters to be larger than 4 GeV and the transverse momentum (P_t^{HCAL}) calculated including the hadron calorimeter clusters to be larger than 5 GeV. Although most of the events from two-photon processes were rejected by the P_t cut, the P_t^{HCAL} cut was applied to reject occasional events with a high transverse momentum neutral hadron. The distributions of transverse momentum after cut (B3) are plotted in Fig. 5a for the data and the simulated background events and in Fig. 5b for the simulated L^+L^- events.

(B5) "Radiative return" events from $e^+e^- \to Z\gamma$, where the γ escaped close to the beam direction, were rejected by requiring that the polar angle of the missing momentum direction θ_{miss} satisfies $|\cos\theta_{miss}| < 0.7$. In Fig. 6, the $|\cos\theta_{miss}|$ distributions are shown just before the cut.

case (B)	data	total bkg.	$q\bar{q}(\gamma)$	$\ell\ell(\gamma)$	'$\gamma\gamma$'	4-f	L^+L^-		
m_{L^-} (GeV)							75	75	65
m_{ν_L} (GeV)							40	70	55
no cuts	−	−	459.5	2630	67686	62.0	1000	1000	1000
cut (B1)	73.4k	28.0k	446.8	368.3	27.1k	26.3	982	951	970
cut (B2)	47.4k	18.7k	332.6	335.3	18.0k	19.0	948	942	933
cut (B3)	33.9k	10.3k	299.7	313.0	9706	16.7	864	878	862
cut (B4)	354	299.2	148.6	130.5	8.46	11.6	821	223	631
cut (B5)	108	107.4	53.1	43.5	3.35	7.47	610	214	526
cut (B6)	7	8.76	0.34	4.31	3.27	0.84	557	214	526
cut (B7)	4	5.71	0.28	3.37	1.53	0.53	490	126	370
cut (B8)	1	2.78	0.25	0.87	1.47	0.19	426	126	368
cut (B9)	0	0.46	0.13	0.09	0.16	0.08	375	111	306
cut (B10)	0	0.12	0.01	0.02	0.02	0.07	334	107	277

Table 3: *The numbers of events remaining, normalised to the integrated luminosity of the data for various background processes are compared with data (corresponding to 3.12 pb^{-1}) after each cut for the $L^- \to \nu_L W^{*-}$ case. Numbers of expected events are also given for three samples of simulated L^+L^- events (starting from 1000 events in each sample). The numbers of events expected from two-photon processes ('$\gamma\gamma$') do not include the region $M_{\gamma\gamma}^2 < 4$ GeV^2 with $Q^2 < 1.0$ GeV^2, which explains the difference between data and Monte Carlo before cut (B4).*

(B6) A visible energy cut was applied to reduce both multihadron and four-fermion background. The visible energy of L^+L^- events was expected to be smaller than about 80 GeV, since the two heavy ν_L's carry away a significant fraction of the energy. The visible energy was required to be smaller than $0.45\sqrt{s}$. The visible energy distributions before this cut are shown in Fig. 7.

(B7) In order to reduce the remaining two-photon processes and multihadron backgrounds, two requirements were adopted:

$$\frac{E(|\cos\theta|>0.8)}{E_{\rm vis}} < 1.5 \, \frac{E_{\rm vis}}{\sqrt{s}},$$

$$|P_{(z)}^{mis}| < 0.4 \, E_{\rm vis},$$

where $E(\cos\theta>0.8)$ is the sum of the visible energy over $|\cos\theta| > 0.8$ and $|P_{(z)}^{mis}|$ is the missing momentum along the beam direction. The scatter plots of $E(|\cos\theta|>0.8)/E_{\rm vis}$ against visible energy, normalized to the centre-of-mass energy, are displayed in Fig. 8. The $|P_{(z)}^{mis}|/E_{\rm vis}$ distributions after cut (B6) are plotted in Fig. 9.

(B8) $\tau^+\tau^-(\gamma)$ and background events from four-fermion processes were rejected by requiring the maximum momentum of tracks to be less than 20 GeV. The maximum track momentum distributions after cut (B7) are shown in Fig. 10.

(B9) In order to reject events containing two back-to-back jets or leptons, the thrust of the events was required to be less than 0.9. The thrust distributions just before the cut are shown in Fig. 11.

(B10) The tracks and the clusters in an event were divided into two hemispheres defined by the plane perpendicular to the thrust axis. The acoplanarity angle $\phi_{\rm acop}$ was defined as $\pi - \phi_{\rm open}$,

where ϕ_{open} is the azimuthal opening angle between the directions of the momentum sums of the particles in the two thrust hemispheres. If all the visible decay products of L^- and L^+ happened to be in the same hemisphere, the event topology could be a monojet and ϕ_{acop} was defined as $180°$. The acoplanarity angle (ϕ_{acop}) between the two jets was required to be greater than $15°$. The acoplanarity angle distributions just before the cut are shown in Fig. 12.

	$m_{\mathrm{L}^-} = 65$ GeV	70 GeV	75 GeV	80 GeV
$m_{\nu_{\mathrm{L}}} = 75$ GeV	–	–	–	10.0 ± 0.9
70 GeV	–	–	10.7 ± 1.0	34.1 ± 1.5
65 GeV	–	9.4 ± 0.9	29.4 ± 1.4	37.0 ± 1.5
60 GeV	10.8 ± 1.0	28.7 ± 1.4	37.5 ± 1.5	41.8 ± 1.6
55 GeV	27.7 ± 1.4	34.8 ± 1.5	40.2 ± 1.6	43.5 ± 1.6
50 GeV	36.6 ± 1.5	39.0 ± 1.5	41.4 ± 1.6	43.5 ± 1.6
45 GeV	35.3 ± 1.5	38.0 ± 1.5	40.9 ± 1.6	36.7 ± 1.5
40 GeV	32.9 ± 1.5	34.6 ± 1.5	33.4 ± 1.5	28.2 ± 1.4

Table 4: *The selection efficiencies (in %) for $L^+L^- \to \nu_{\mathrm{L}}W^{*+}\nu_{\mathrm{L}}W^{*-}$ candidates on the mass combinations between m_{L^-} and $m_{\nu_{\mathrm{L}}}$ in this analysis. The errors are statistical only.*

No event was observed in the data after the above selection. These results were consistent with the expected background from all sources of 0.12 events.

The detection efficiencies for L^+L^- events are summarized in table 4.

3.3 Selection of $L^+L^- \to \nu_\ell W^{*+}\nu_\ell W^{*-}$ candidates (case C)

The number of events remaining after each cut are listed in Table 5 for case (C). For comparison the table also includes the corresponding numbers of simulated background and L^+L^- events.

The following selection criteria were applied:
(C1) The number of tracks was required to be at least five, and the ratio of the number of tracks which satisfied the selection criteria to the total number of reconstructed tracks was required to be larger than 0.2 in order to reject beam-gas and beam-wall backgrounds.

(C2) The criteria for energy deposits in the silicon tungsten calorimeter, the forward calorimeter and the gamma-catcher were identical to those in the $L^0\bar{L}^0$ analysis.

(C3) The cosine of the polar angle of the thrust axis ($|\cos\theta_{\mathrm{thrust}}|$) was required to be less than 0.95 in order to reduce beam-gas and beam-wall background events as well as events from two-photon processes.

(C4) The transverse momentum was expected to be large for the expected signals, hence P_t and P_t^{HCAL} were required to be larger than 12 GeV and 15 GeV, respectively. With this cut two-photon process backgrounds were effectively reduced.

(C5) "Radiative return" events from $e^+e^- \to Z\gamma$, where the γ escaped close to the beam direction, were rejected by requiring that the polar angle of the missing momentum direction θ_{miss} satisfy $|\cos\theta_{\mathrm{miss}}| < 0.9$. The $|\cos\theta_{\mathrm{miss}}|$ cut was looser than in case (B) because the P_t and P_t^{HCAL} cuts in case (C) were higher than in case (B).

8

case (C)	data	total bkg.	$q\bar{q}(\gamma)$	$\ell\ell(\gamma)$	'$\gamma\gamma$'	4-f	L^+L^-	
m_{L^-} (GeV)							65	75
no cuts	–	–	459.5	2630	67686	62.0	1000	1000
cut (C1)	11.7k	11.4k	445.2	5.42	10.9k	19.0	880	890
cut (C2)	6301	6284	332.4	4.85	5932	14.9	799	827
cut (C3)	3624	3535	321.5	4.67	3195	14.3	761	804
cut (C4)	41	34.6	28.2	1.23	0.52	4.69	574	611
cut (C5)	32	27.4	21.6	1.09	0.17	4.52	553	599
cut (C6)	12	10.8	7.23	0.20	0.05	3.29	506	524
(HL)	1	3.23	1.04	0.07	0.00	2.12	234	241
cut (HL7)	0	0.25	0.12	0.02	0.00	0.11	138	146
cut (HL8)	0	0.11	0.00	0.01	0.00	0.10	130	133
(HH)	3	1.70	1.29	0.00	0.00	0.41	141	168
cut (HH9)	2	0.68	0.47	0.00	0.00	0.21	122	156
cut (HH10)	2	0.40	0.22	0.00	0.00	0.18	113	147
cut (HH11)	2	0.27	0.15	0.00	0.00	0.12	98	136
cut (HH12)	0	0.11	0.02	0.00	0.00	0.09	74	102
(HL8)+(HH11)	0	0.22	0.02	0.01	0.00	0.19	204	235

Table 5: *The numbers of events remaining, normalised to the integrated luminosity, for various background processes are compared with data (corresponding to 3.12 pb^{-1}) after each cut for the $L^- \to \nu_\ell W^{*-}$ case. Numbers of expected events are also given for three samples of simulated L^+L^- events (starting from 1000 events in each sample). The numbers of events expected from two-photon processes ('$\gamma\gamma$') do not include the region $M_{\gamma\gamma}^2 < 4$ GeV^2 with $Q^2 < 1.0$ GeV^2.*

(C6) In order to reject events containing two back-to-back jets or leptons, the thrust of the events was required to be less than 0.9.

The remaining events were classified into two categories (HL, HH):

- If there was one lepton (e, μ or τ) which had a momentum larger than 8 GeV and three reconstructed jets, these events were categorized as (HL) events, where the lepton identification is identical to the $L^0\bar{L}^0$ case.

- If there was no track identified as a lepton which had a momentum larger than 8 GeV, and the number of jets was four, events were categorized as (HH) events.

The events which were not assigned as (HL) or (HH) events were rejected in order to reduce multihadron and four-fermion backgrounds. The expected signal topologies are $L^+L^- \to \nu_\ell W^{*-}\nu_\ell W^{*+} \to \nu_\ell\nu_\ell\ell\nu_\ell qq'$, $\nu_\ell\nu_\ell qq'q''q'''$ or $\nu_\ell\nu_\ell\ell\nu_\ell\ell\nu_\ell$, hence $\nu_\ell\nu_\ell\ell\nu_\ell qq'$ and $\nu_\ell\nu_\ell qq'q''q'''$ events are effectively categorized into (HL) and (HH) with this selection.

(HL7) For (HL) events the visible energy was required to be smaller than $0.6\sqrt{s}$ and larger than $0.25\sqrt{s}$. With this cut four-fermion processes and multihadron backgrounds were sufficiently reduced. Visible energy distributions normalized to $\sqrt{s}$ for the (HL) events after cut (C5) are shown in Fig. 13.

(HL8) The acoplanarity angle (ϕ_{acop}) was required to be greater than $10°$ to reject multihadron events. The calculation of the acoplanarity angle is identical to cut (B10). The acoplanarity angle distributions just before the cut are plotted in Fig. 14.

(HH9) For (HH) events the visible energy was required to be smaller than $0.9\sqrt{s}$ and larger than $0.4\sqrt{s}$. Multihadron backgrounds were reduced by this cut. Visible energy distributions normalized to $\sqrt{s}$ for the (HH) events after cut (C5) are shown in Fig. 15.

(HH10) The remaining background comes primarily from hadronic events in which a mis-measurement of the energy of a jet leads to an artificial missing momentum. This missing momentum tends to lie along the direction of jets in ordinary multihadron events. We defined the total energy sum (E_{back}) within a cone of $20°$ half-angle around the direction of the missing momentum. E_{back} was required to be less than 5 GeV in order to reduce a large fraction of multihadron background. The E_{back} distributions after cut (HH8) are shown in Fig. 16.

(HH11) Four-fermion processes and multihadron background were rejected by requiring the maximum momenta of tracks to be less than 30 GeV. Distributions of the maximum charged track momentum after cut (HH10) are shown in Fig. 17.

(HH12) The acoplanarity angle (ϕ_{acop}) was required to be greater than $15°$ to reject multihadron events. The acoplanarity angle distributions just before the cut are plotted in Fig. 18.

$m_{\mathrm{L}^-} = 60$ GeV	65 GeV	70 GeV	75 GeV	80 GeV
19.6 ± 1.3	20.4 ± 1.3	23.9 ± 1.3	23.5 ± 1.3	17.9 ± 1.2

Table 6: *The selection efficiencies (in %) of* $\mathrm{L}^- \to \nu_\ell \mathrm{W}^{*-}$ *candidates as a function of mass. The errors are statistical only.*

No event was observed in the data after the above selections. These results are consistent with the expected background from all sources of 0.22 events.

The detection efficiencies for $\mathrm{L}^+\mathrm{L}^-$ events are summarized in table 6.

4   Mass Limits

The expected numbers of neutral and charged heavy lepton events were estimated for various values for heavy lepton mass (or combinations of (m_{L^-}, $m_{\nu_{\mathrm{L}}}$)) using the detection efficiency at each centre-of-mass energy, the cross-section and integrated luminosity. In the calculation of limits the detection efficiency at arbitrary values of the heavy lepton masses was interpolated using a polynomial fit.

The systematic errors on the total number of expected signal events were estimated to be 3-6% from Monte Carlo statistics, depending on the event topology, 0.2% (0.1%) from the uncertainty on the beam energy estimation for $\mathrm{L}^0\bar{\mathrm{L}}^0$ ($\mathrm{L}^+\mathrm{L}^-$), 1.0% from the interpolation of the efficiencies, 0.9% from the uncertainty in the integrated luminosity measured by SW, 3.7% from the lepton identification uncertainty, and 1.6% (0.9%) from the uncertainty in the fragmentation of W^* hadronic decays for $\mathrm{L}^0\bar{\mathrm{L}}^0$ ($\mathrm{L}^+\mathrm{L}^-$). The fragmentation errors arose through the jet reconstruction and lepton isolation uncertainties for the $\mathrm{L}^0\bar{\mathrm{L}}^0$ case and mainly through the uncertainty in the estimation of the acoplanarity angle and the missing momentum direction for the $\mathrm{L}^+\mathrm{L}^-$ case. The fragmentation error was estimated by varying the optimized fragmentation

parameters [24] in the JETSET 7.4 Monte Carlo generator. The systematic error due to trigger efficiency was estimated to be negligible for the selected signal events. In calculating the mass limits the systematic errors were treated as described in Ref. [25] and were considered to be independent.

The mass limits were calculated by combining the numbers of expected events from the $\sqrt{s} = 130$ and 136 GeV analysis [4]. A 95% C.L. lower limit of 64.5 GeV is obtained for the Dirac neutral heavy lepton mass, assuming that both L^0 and $\bar{L}^0$ decay into eW^* with 100% branching fraction. The mass limits for the cases of $L^0 \to \mu W^*$ and $L^0 \to \tau W^*$ are 64.6 GeV and 60.8 GeV, respectively. For Majorana L^0 the limits are reduced to 54.5 GeV for the eW^* decay, 55.3 GeV for μW^* decay and 50.1 GeV for τW^* decay due to the smaller cross-section near the $L^0 \bar{L}^0$ threshold. The expected number of signal events as a function of m_{L^0} are plotted in Fig. 19.

The mass of the $L^{\pm}$ was found to be larger than 67.5 GeV at 95% C.L. for case (B), if $m_{L^-} - m_{\nu_L} > 10$ GeV. The excluded region in the (m_{L^-}, m_{ν_L}) plane for case (B) is presented in Fig. 20. For case (C) the lower limit for m_{L^-} is 66.0 GeV at 95% C.L. The expected number of signal events as a function of m_{L^-} in case (C) are plotted in Fig. 21.

The lower mass limits on the LEP1.5 data and the $\sqrt{s} \approx 161$ GeV data combined with LEP1.5 data for each case were summarized in Table. 7.

Event topology		LEP1.5 data	LEP1.5+$\sqrt{s} \approx 161$ GeV data
$L^0 \bar{L}^0 \to eW^* eW^*$	Dirac	62.5 GeV	64.5 GeV
	Majorana	51.4 GeV	54.5 GeV
$L^0 \bar{L}^0 \to \mu W^* \mu W^*$	Dirac	63.0 GeV	64.6 GeV
	Majorana	52.2 GeV	55.3 GeV
$L^0 \bar{L}^0 \to \tau W^* \tau W^*$	Dirac	57.4 GeV	60.8 GeV
	Majorana	44.2 GeV	50.1 GeV
$L^- \to \nu_L W^{*-}$		64.5 GeV	67.5 GeV
$L^- \to \nu_\ell W^{*-}$		63.9 GeV	66.0 GeV

Table 7: *The lower mass limits for new unstable heavy leptons on LEP1.5 data and $\sqrt{s} \approx 161$ GeV data combined with LEP1.5 data. The mass limits for $L^- \to \nu_L W^{*-}$ case were assumed to be $m_{L^-} - m_{\nu_L} > 10$ GeV.*

5   Summary and Conclusions

A search has been made for pair production of unstable neutral and charged heavy leptons using a data sample corresponding to an integrated luminosity of 3.12 pb^{-1} at $\sqrt{s} \approx 161$ GeV, collected with the OPAL detector at LEP. No event remained after the selection cuts, consistent with the expected number of background events.

The 95% C.L. lower limit on the Dirac L^0 mass, assuming that L^0 decays into eW^* with 100% branching fraction, was obtained to be 64.5 GeV. The mass limits for μW^* and τW^* decays are 64.6 GeV and 60.8 GeV, respectively. For Majorana L^0 the limits were reduced to

54.5 GeV for pure eW* decay, 55.3 GeV for pure μW* decay and 50.1 GeV for the τW* case due to the smaller cross-section in the region near the L$^0\bar{\text{L}}^0$ threshold.

The excluded region in the (m_{L^-}, $m_{\nu_{\text{L}}}$) plane is presented in Fig. 18. If $m_{\text{L}^-} - m_{\nu_{\text{L}}} >$ 10 GeV, the mass of L$^-$ was found to be larger than 67.5 GeV at 95% C.L. If $m_{\nu_{\text{L}}} > m_{\text{L}^-}$ and L$^-$ decays into a massless neutrino and a virtual W boson, a lower limit of 66.0 GeV at 95% C.L. was obtained for m_{L^-}. The results of these analyses are consistent with, and in some cases have extended, existing limits from other LEP experiments [3, 4].

References

[1] L. Montanet *et al.*, Phys. Rev. D50 (1994) 1418.

[2] H. Baer *et al.*, in Physics at LEP, vol. 1, eds. J. Ellis
and R. Peccei, CERN-86-02 (1986) 297.

[3] ALEPH Collab., D. Decamp *et al.*, Phys. Lett. B236 (1990) 511;
OPAL Collab., M.Z. Akrawy *et al.*, Phys. Lett. B240 (1990) 250;
OPAL Collab., M.Z. Akrawy *et al.*, Phys. Lett. B247 (1990) 448;
L3 Collab., B. Adeva *et al.*, Phys. Lett. B251 (1990) 321;
OPAL Collab., G. Alexander *et al.*, Z. Phys. C52 (1991) 175;
DELPHI Collab., P. Abreu *et al.*, Phys. Lett. B274 (1992) 230;
L3 Collab., M. Acciarri *et al.*, CERN-PPE/96-038 (1996);
ALEPH Collab., D. Buskulic *et al.*, CERN-PPE/96-080 (1996).

[4] OPAL Collab., G. Alexander *et al.*, CERN-PPE/96-093 (1996).

[5] OPAL Collab., K. Ahmet *et al.*, Nucl. Instr. Meth. A305 (1991) 275;
P. P. Allport *et al.*, Nucl. Instr. Meth. A324 (1993) 34;
P. P. Allport *et al.*, Nucl. Instr. Meth. A346 (1994) 476.

[6] B.E. Anderson *et al.*, IEEE Transactions on Nuclear Science 41 (1994) 845.

[7] S. Jadach and J. Kühn, preprint MPI-PAE/PTh 64/86.

[8] T. Sjöstrand, Comput. Phys. Commun. 82 (1994) 74.

[9] F.A. Berends, R. Kleiss and S. Jadach, Nucl. Phys. B202 (1982) 63;
F.A. Berends, R. Kleiss and S. Jadach, Comp. Phys. Comm. 29 (1983) 185.

[10] T. Sjöstrand,"PYTHIA 5.6 and JETSET 7.4 Physics and Manual", CERN-TH. 7112/93 (1993) and references therein.

[11] S. Jadach, B. F. L. Ward, Z. Wąs, Comp. Phys. Comm. 79 (1994) 503.

[12] S. Jadach, W. Płaczek, B. F. L. Ward, in 'Physics at LEP2', Editted by G. Altarelli, T. Sjöstrand and F. Zwirner, CERN 96-01,vol.2 (1996).

[13] In 'Physics at LEP2', Editted by G. Altarelli, T. Sjöstrand and F. Zwirner, CERN 96-01,vol.2 (1996).

[14] G. Marchesini, B. R. Webber, G. Abbiendi, I. G. Knowles, M. H. Seymour and L. Stanco, Comp. Phys. Comm. 67 (1992) 465.

[15] J. A. M. Vermaseren, Nucl. Phys. B229 (1983) 347.

[16] F.A Berends, R. Kleiss and R. Pittau, Comp. Phys. Comm. 85 (1995) 437.

[17] J. Allison *et al.*, Nucl. Instr. Meth. A317 (1992) 47.

[18] OPAL Collab., G. Alexander *et al.*, CERN-PPE/96-019 (1996).

[19] OPAL Collab., G. Alexander *et al.*, CERN-PPE/96-020 (1996).

[20] S. Catani *et al.*, Nucl. Phys. B269 (1991) 432.

[21] OPAL Collab., R. Akers *et al.*, Phys. Lett. B327 (1994) 411.

[22] OPAL Collab., P. Acton *et al.*, Z. Phys. C58 (1993) 523.

[23] OPAL Collab., R. Akers *et al.*, Z. Phys. C60 (1993) 199.

[24] OPAL Collab., G. Alexander *et al.*, Z. Phys. C69 (1996) 543.

[25] R.D. Cousins and V.L. Highland, Nucl. Inst. and Method A320 (1992) 331.
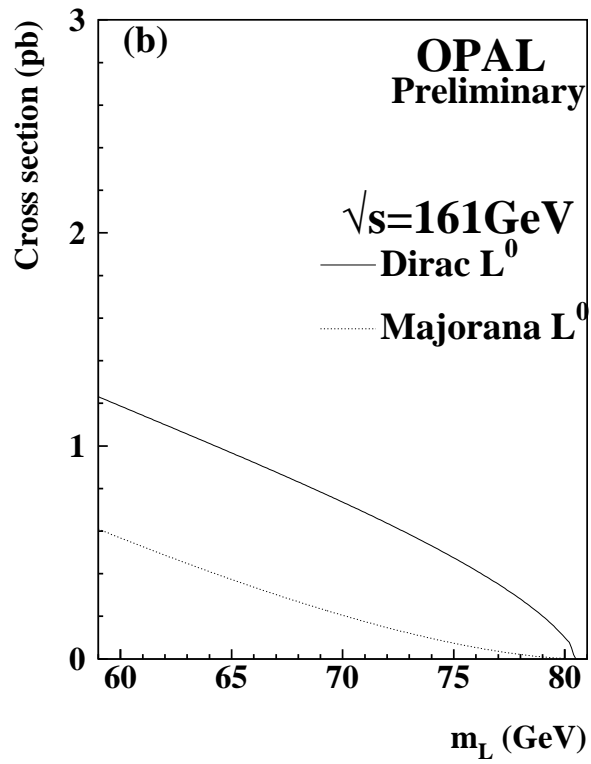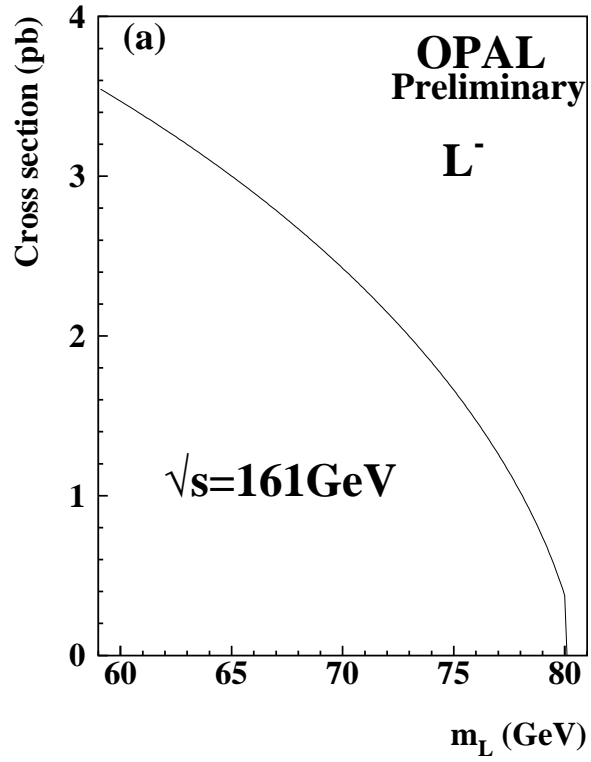
Figure 1: Total cross sections for heavy lepton production including initial state radiation [9] at $\sqrt{s} = 161$ GeV.
(a) Charged heavy lepton,
(b) neutral heavy lepton.
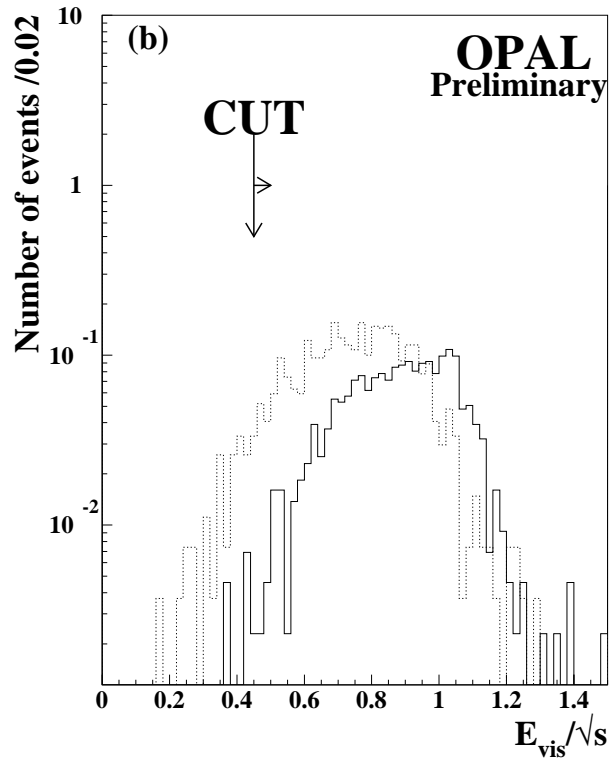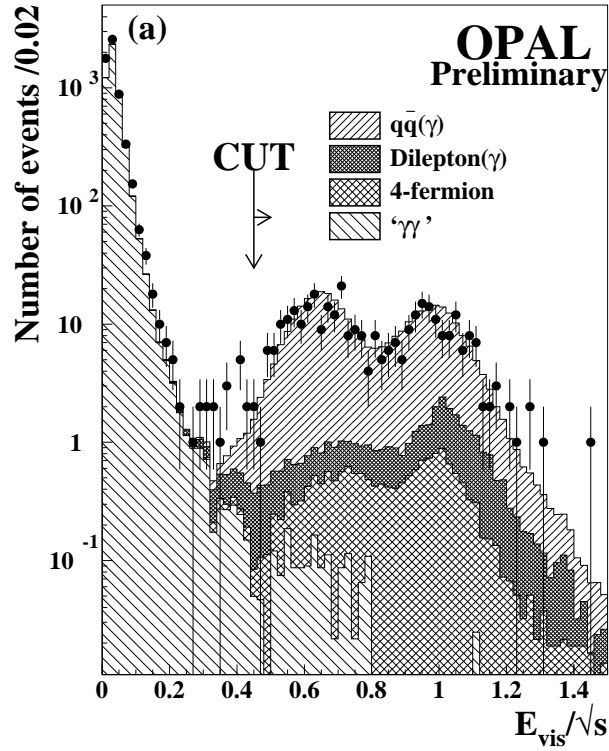
Figure 2: The distributions of the visible energy normalised to $\sqrt{s}$ after cut (A3) for the data (bold circles with error bars) and for the simulated background events are plotted in (a). The symbols used for the various backgrounds are explained in (a). The same distributions are shown in (b) for simulated $L^0\bar{L}^0 \to eW^*eW^*$ events with $m_{L^0} = 75$ GeV (solid line histogram) and $L^0\bar{L}^0 \to \tau W^*\tau W^*$ events with $m_{L^0} = 60$ GeV (dotted line histogram).

15
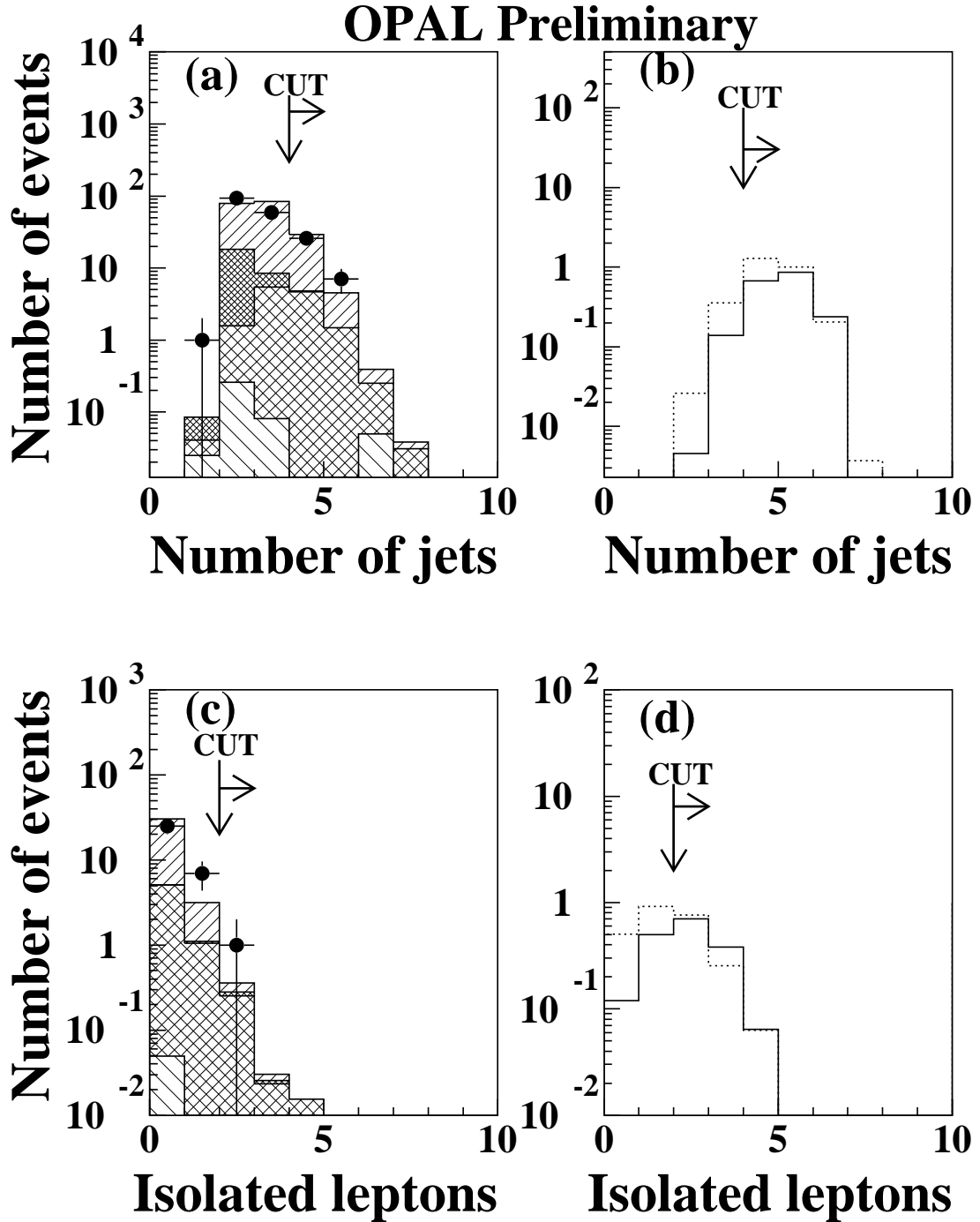
Figure 3: The distributions of the number of jets after cut (A5) for the data (bold circles with error bars) and for the simulated background events are plotted in (a). The same distributions are shown in (b) for simulated $L^0\bar{L}^0 \to eW^*eW^*$ events with $m_{L^0} = 75$ GeV (solid line histogram) and $L^0\bar{L}^0 \to \tau W^*\tau W^*$ events with $m_{L^0} = 60$ GeV (dotted line histogram). The distributions of the number of isolated leptons after cut (A6) for the data and the simulated background events are displayed in (c). The distributions of the number of isolated leptons for the $L^0\bar{L}^0$ events are shown in (d) for the same samples as (b). The convention for indicating the background sources and the figure definition are the same as in Fig. 2.
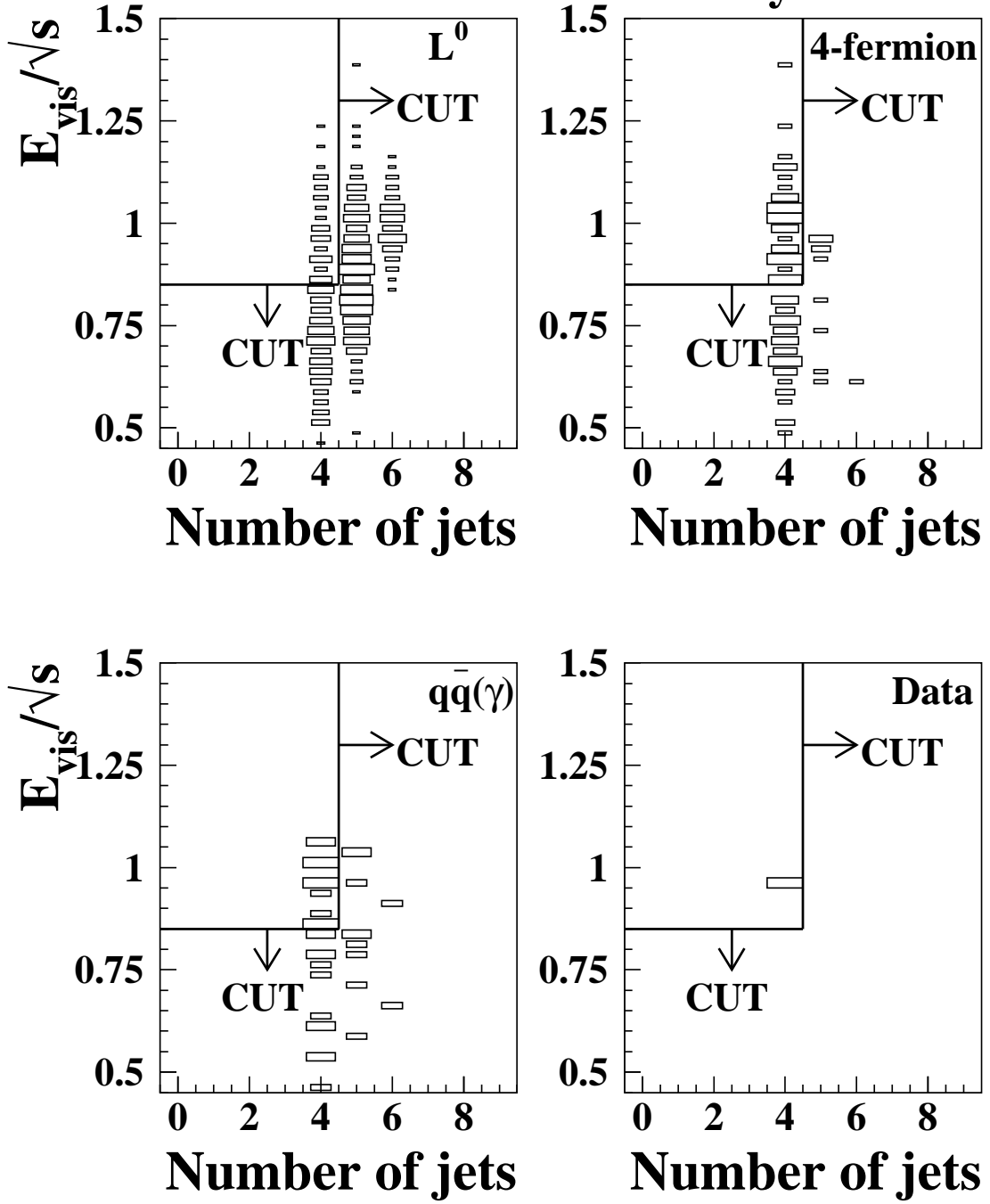
Figure 4: Box distributions of the number of jets and visible energy normalized to the centre-of-mass energy after cut (A7). For the expected signal events (L^0), the the dependence of the visible energy on the number of jets arises because the expected events topologies are $L^0 L^0 \to \ell^- W^{*+} \ell^+ W^{*-} \to \ell\ell\ell\nu_\ell\ell\nu_\ell$ (4jets), $\ell\ell\ell\nu_\ell qq'$ (5 jets) or $\ell\ell\ qq'q''q'''$ (6jets).
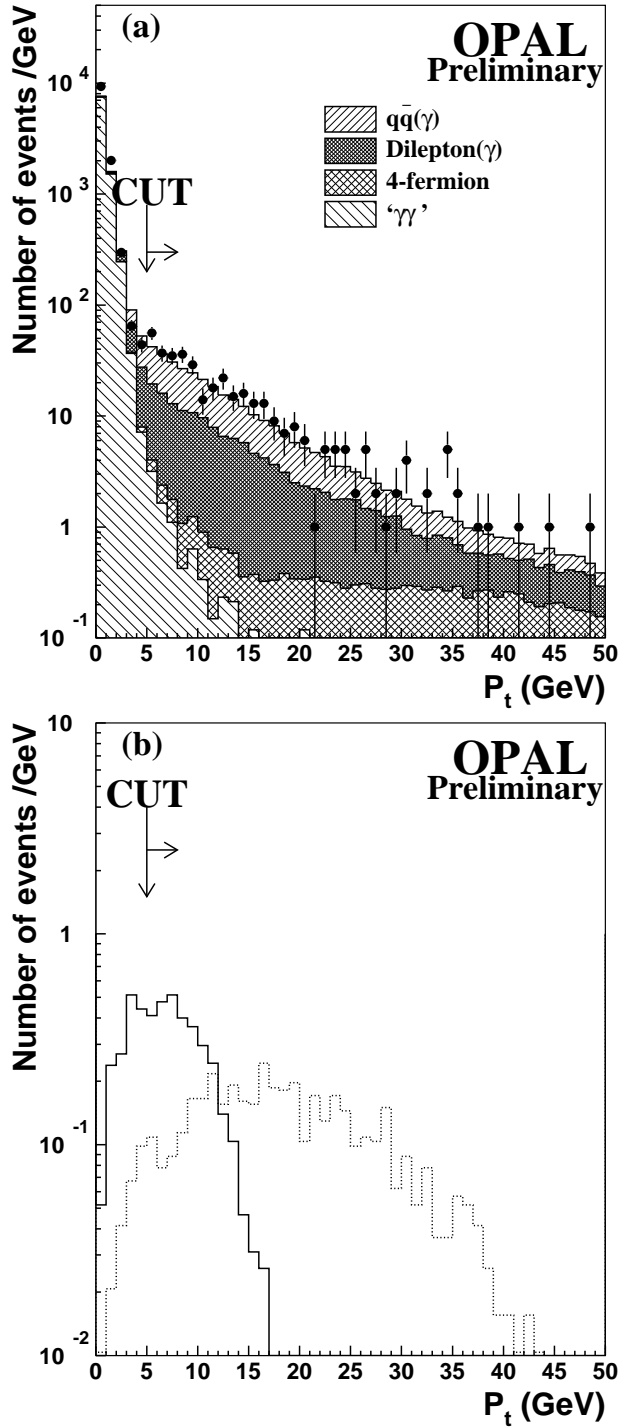
Figure 5: The missing transverse momentum distributions after cut (B3) for the data (bold circles with error bars) and for the simulated background events are plotted in (a). The same distributions are shown in (b) for simulated $L^- \rightarrow \nu_L W^{*-}$ events with $(m_{L^-}, m_{L^0}) = (75,$ 70) GeV (solid line histogram) and $(m_{L^-}, m_{L^0}) = (75, 40)$ GeV (dotted line histogram). Since two-photon Monte Carlo events were generated with $M^2_{\gamma\gamma} > 4$ GeV^2, the visible mass of the events was required to be larger than 2 GeV just for this plot in order to demonstrate that the normalisation of the two-photon events agrees with the Monte Carlo prediction.

18
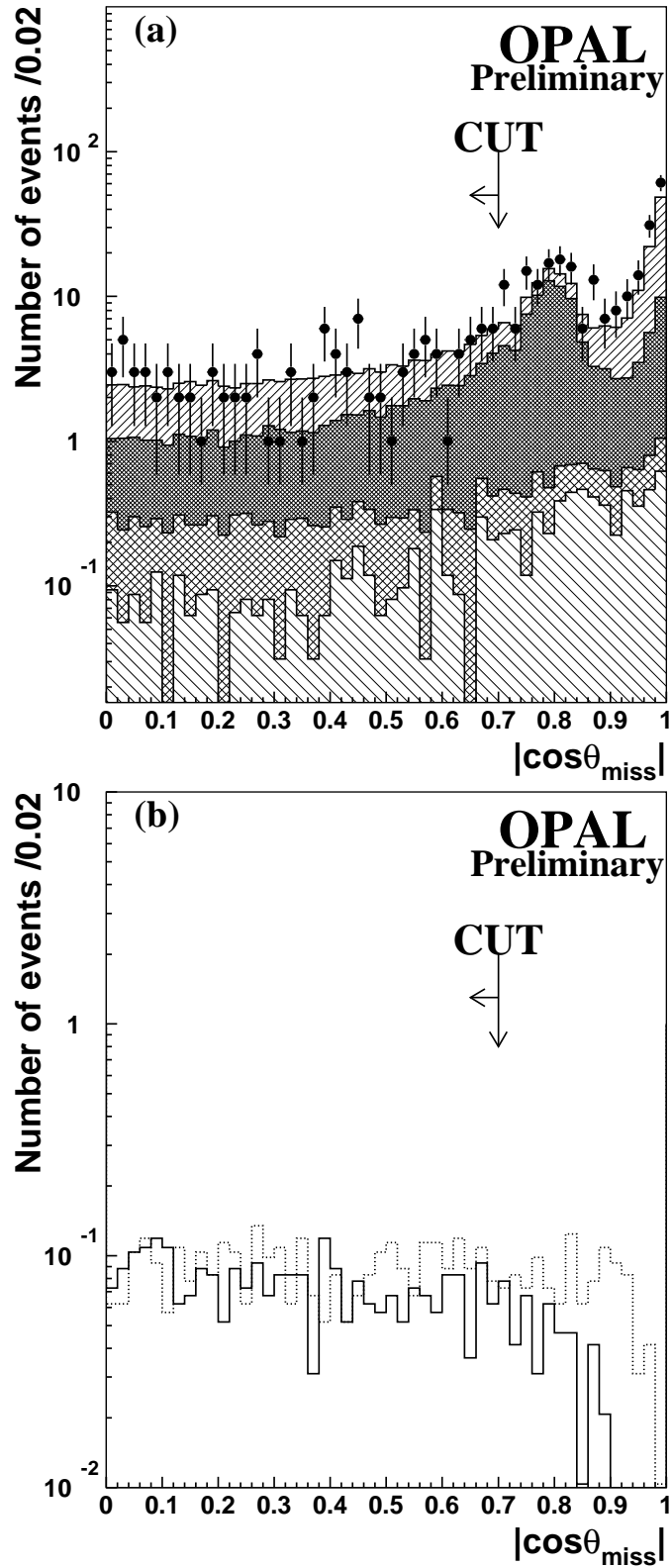
Figure 6: $|\cos\theta_{\mathrm{miss}}|$ distributions after cut (B4). The convention for indicating the background sources in (a) and the expected signal sample in (b) is the same as in Fig. 5. The peak around $|\cos\theta_{\mathrm{miss}}| \approx 0.75$ is due to degraded energy resolution in the region with a larger amount of material in front of the calorimeter.
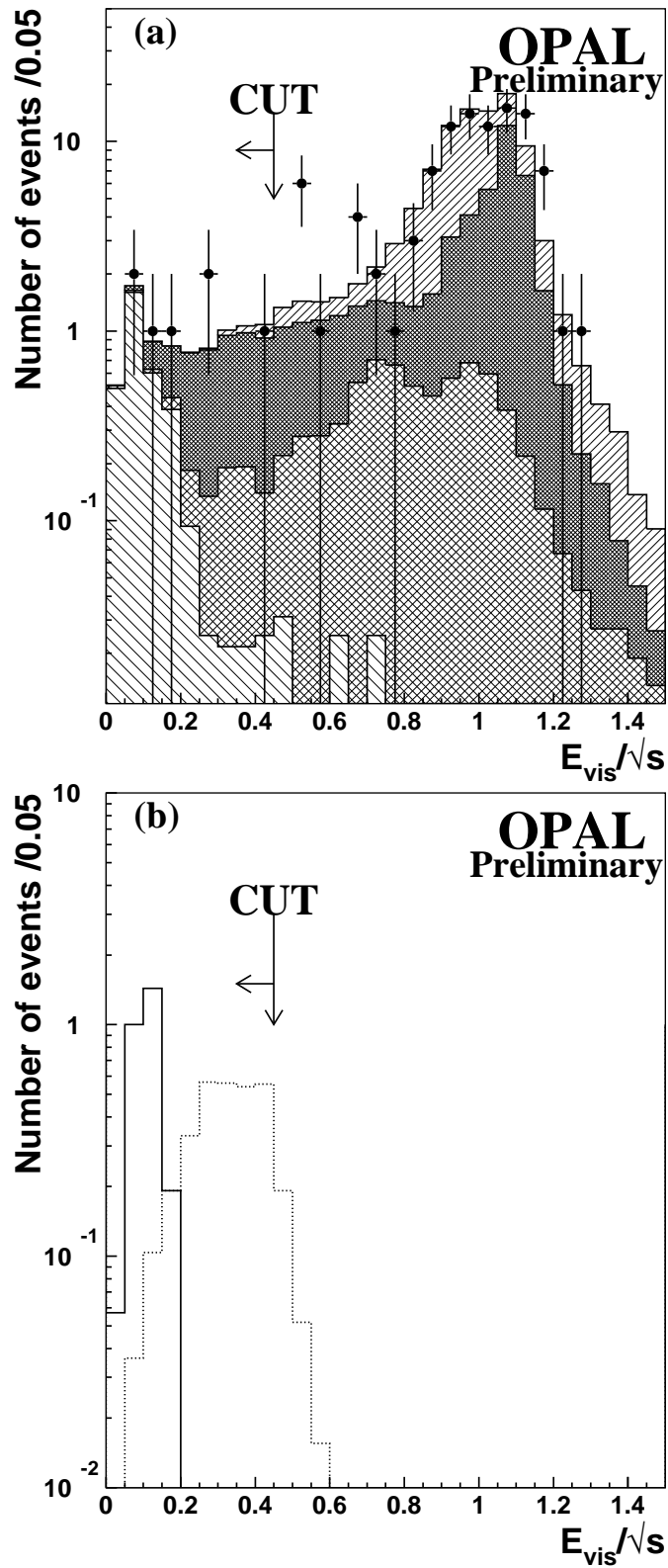
Figure 7: Visible energy distributions normalised to $\sqrt{s}$ after cut (B5). The convention for indicating the background sources in (a) and the figure definition are the same as in Fig. 5.
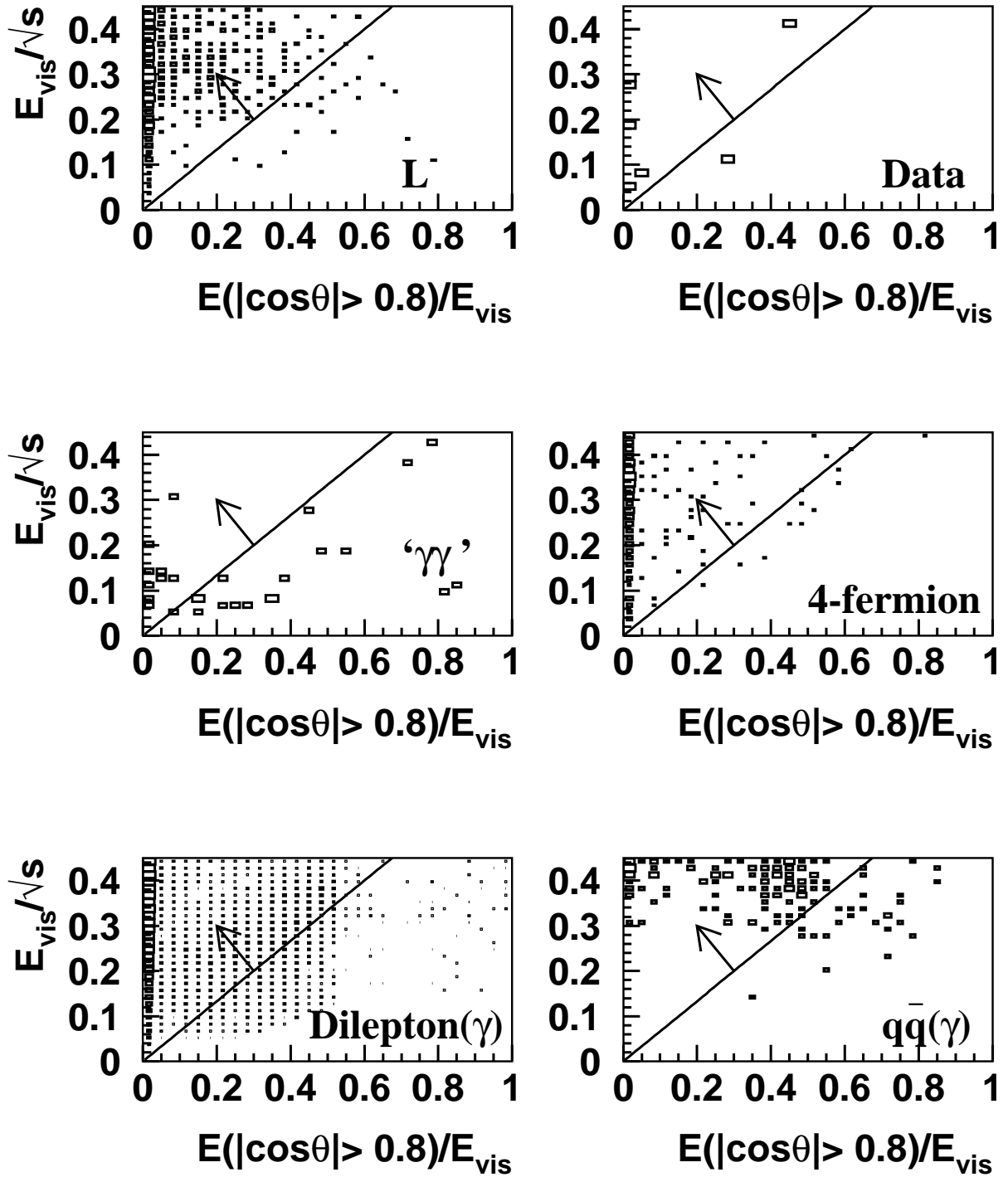
Figure 8: Scatter plots showing $E(|\cos\theta|>0.8)/E_{vis}$ vs. the visible energy (E_{vis}), normalised to $\sqrt{s}$, after cut (B6). The diagonal line indicates cut (B7).
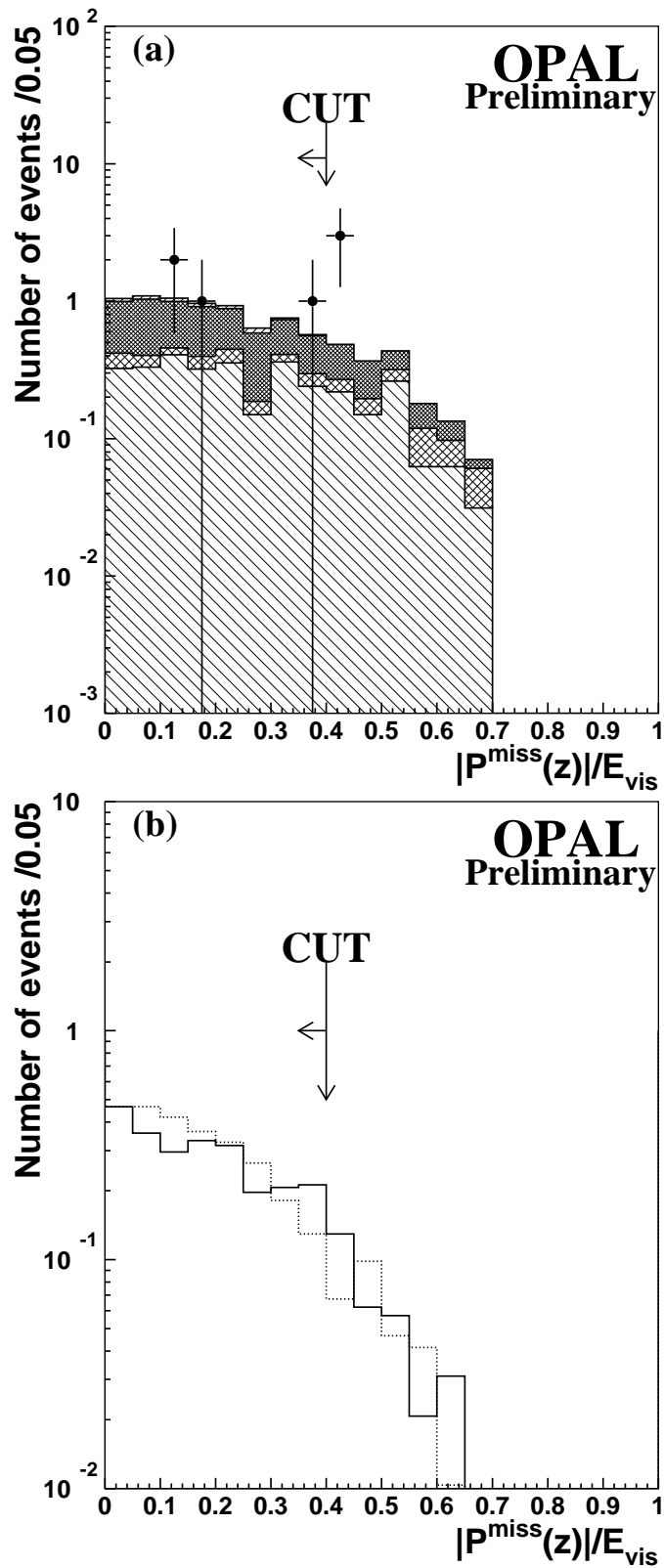
Figure 9: The $\left|P_{(z)}^{mis}\right|$, normalized to visible energy, distributions after cut (B6). The convention for indicating the background sources in (a) and the expected signal sample in (b) are the same as in Fig. 5.
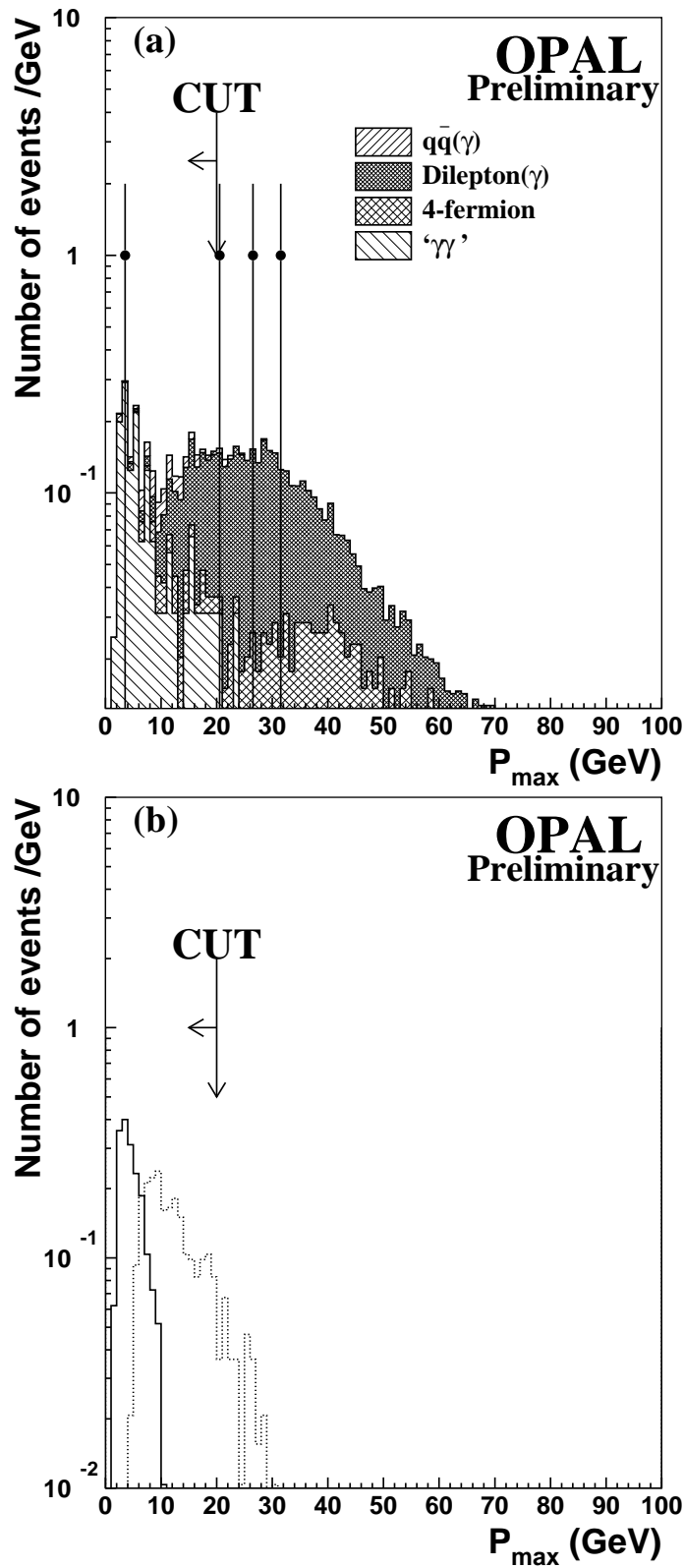
Figure 10: The maximum charged track momentum distributions after cut (B7). The convention for indicating the expected signal sample in (b) are the same as in Fig. 5.
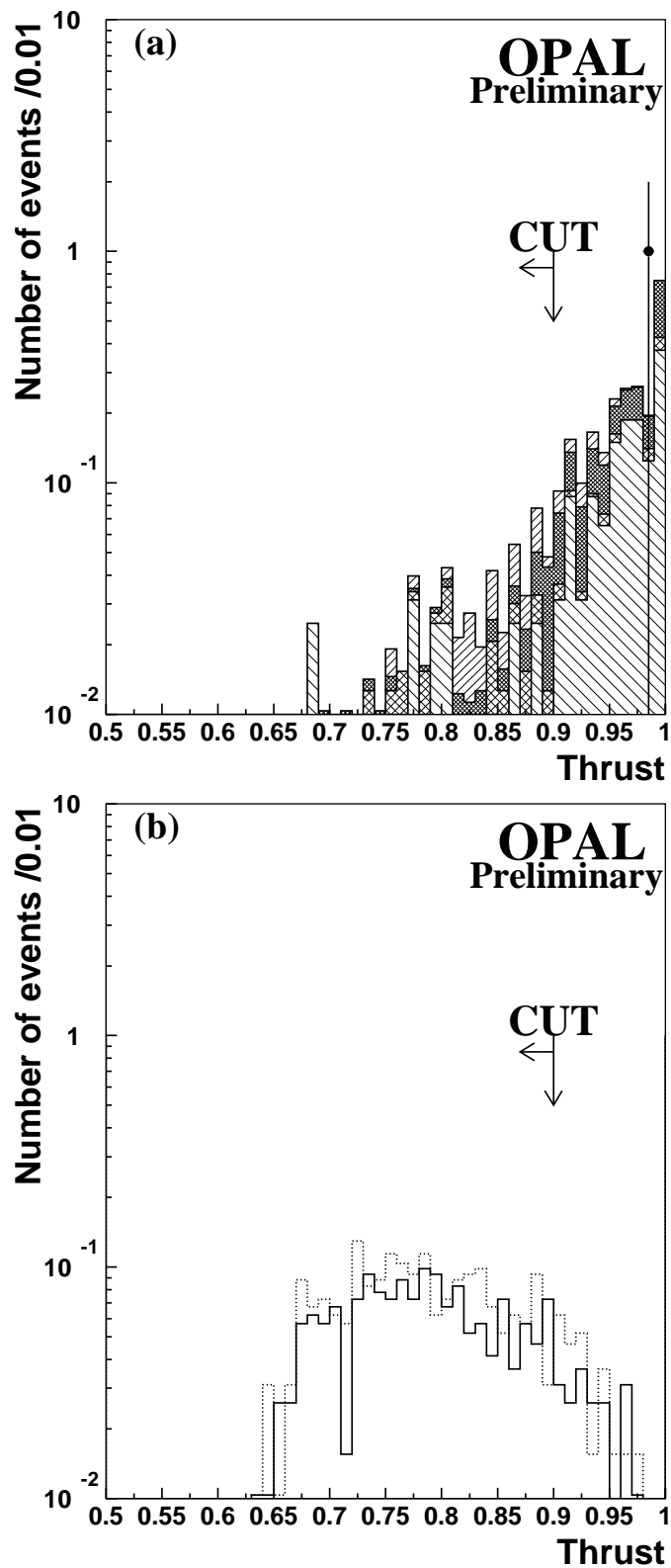
Figure 11: Thrust distributions for the dijet events after cut (B8). The convention for indicating the background sources in (a) and the expected signal sample in (b) are the same as in Fig. 5.
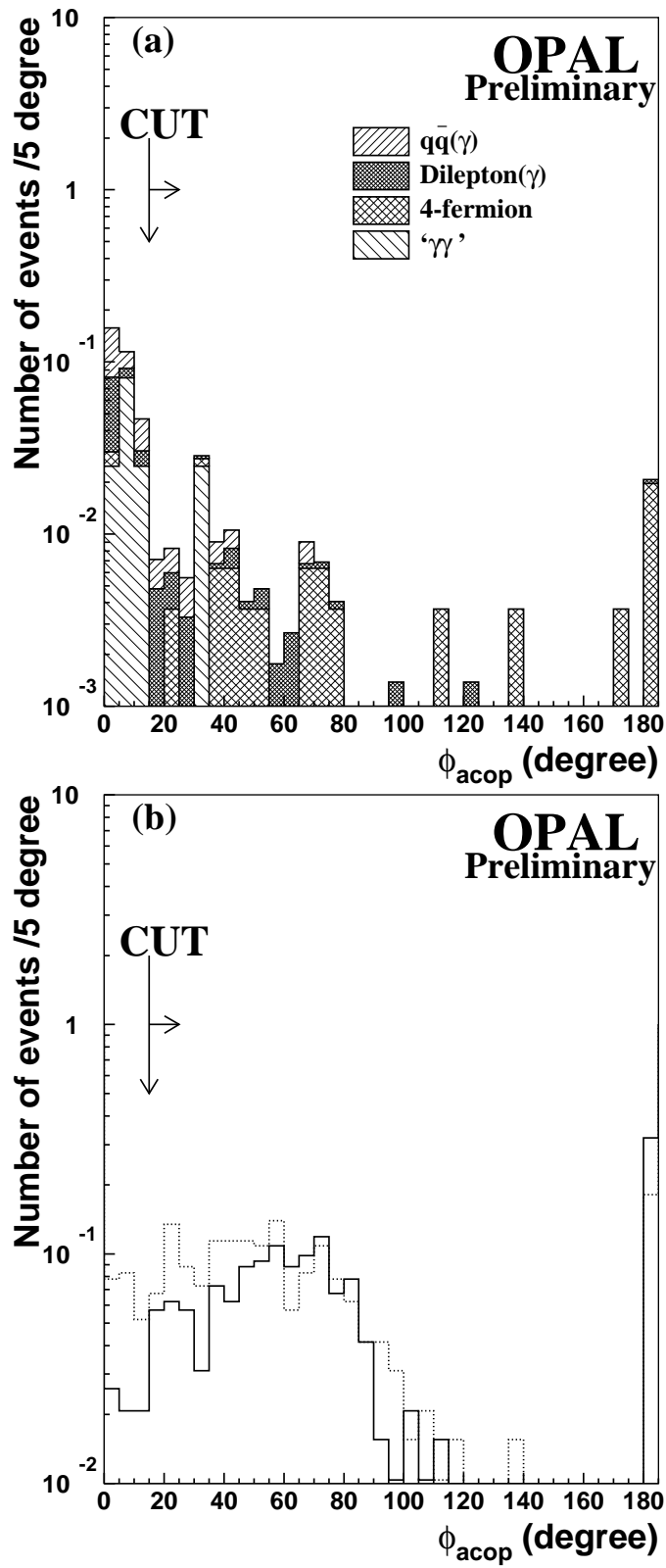
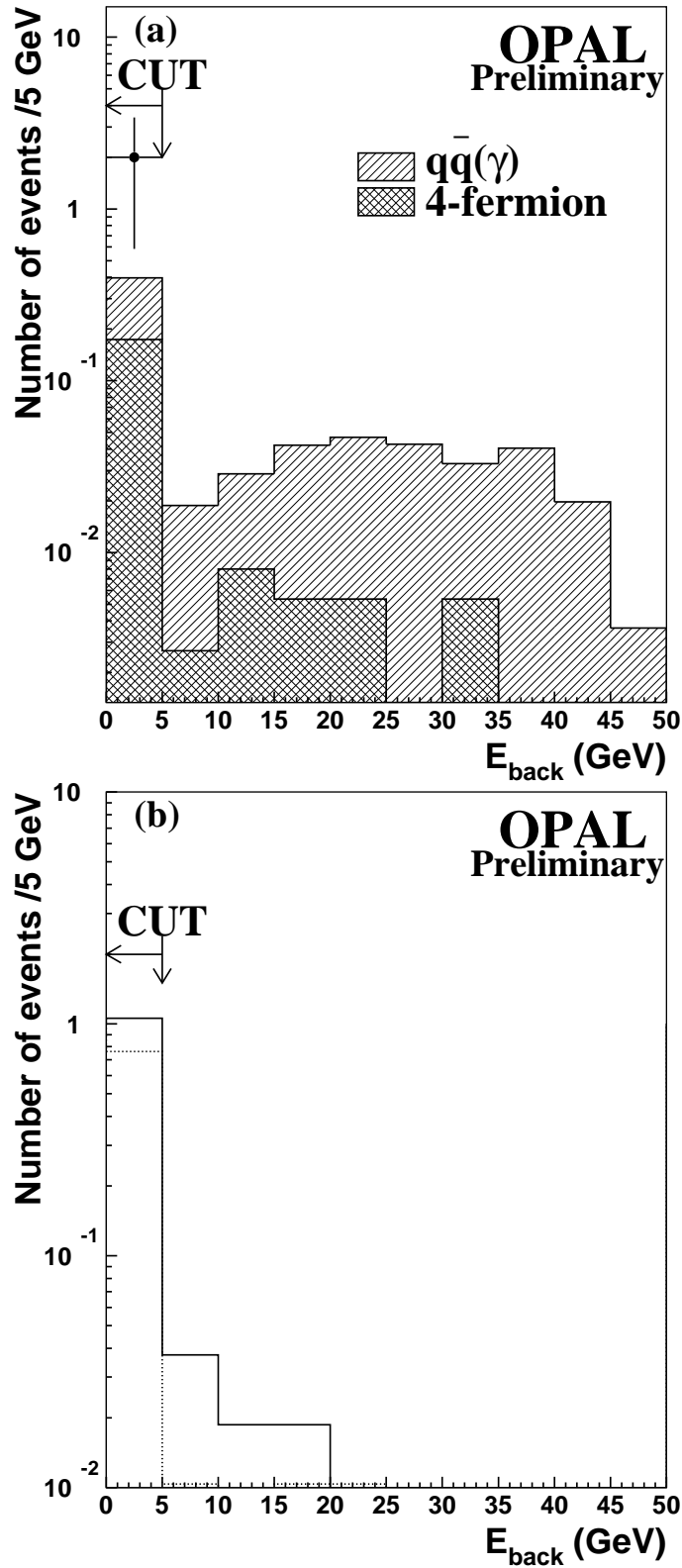Figure 12: Acoplanarity angle distributions after cut (B9) for the $L^- \to \nu_L W^{*-}$ case. The convention for indicating the expected signal sample in (b) are the same as in Fig. 5.
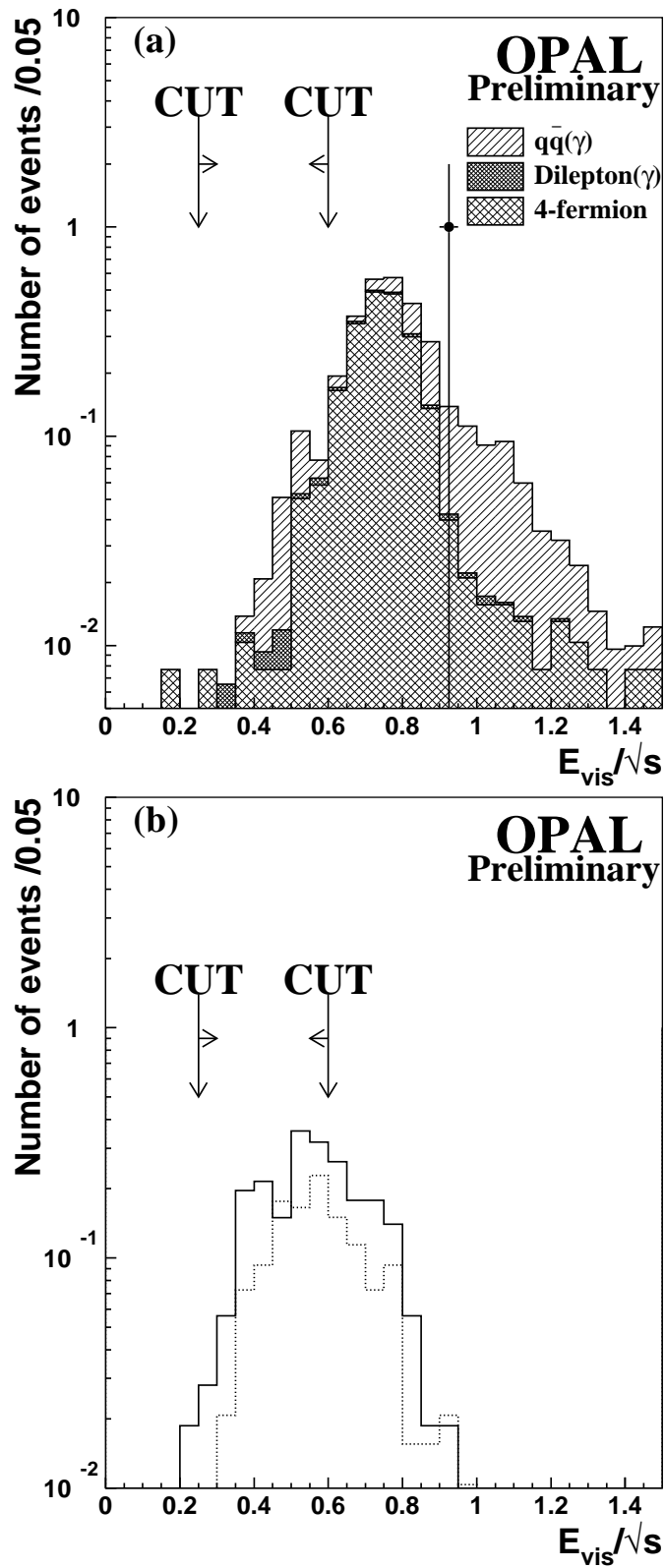
Figure 13: Visible energy distributions for (HL) events normalised to $\sqrt{s}$ after cut (C6). The convention for indicating the background sources in (a) and the figure definition are the same as in Fig. 5. The dashed and dotted histograms in (b) represent the L^+L^- Monte Carlo events for $m_{L^-} = 65$ GeV and 75 GeV, respectively.
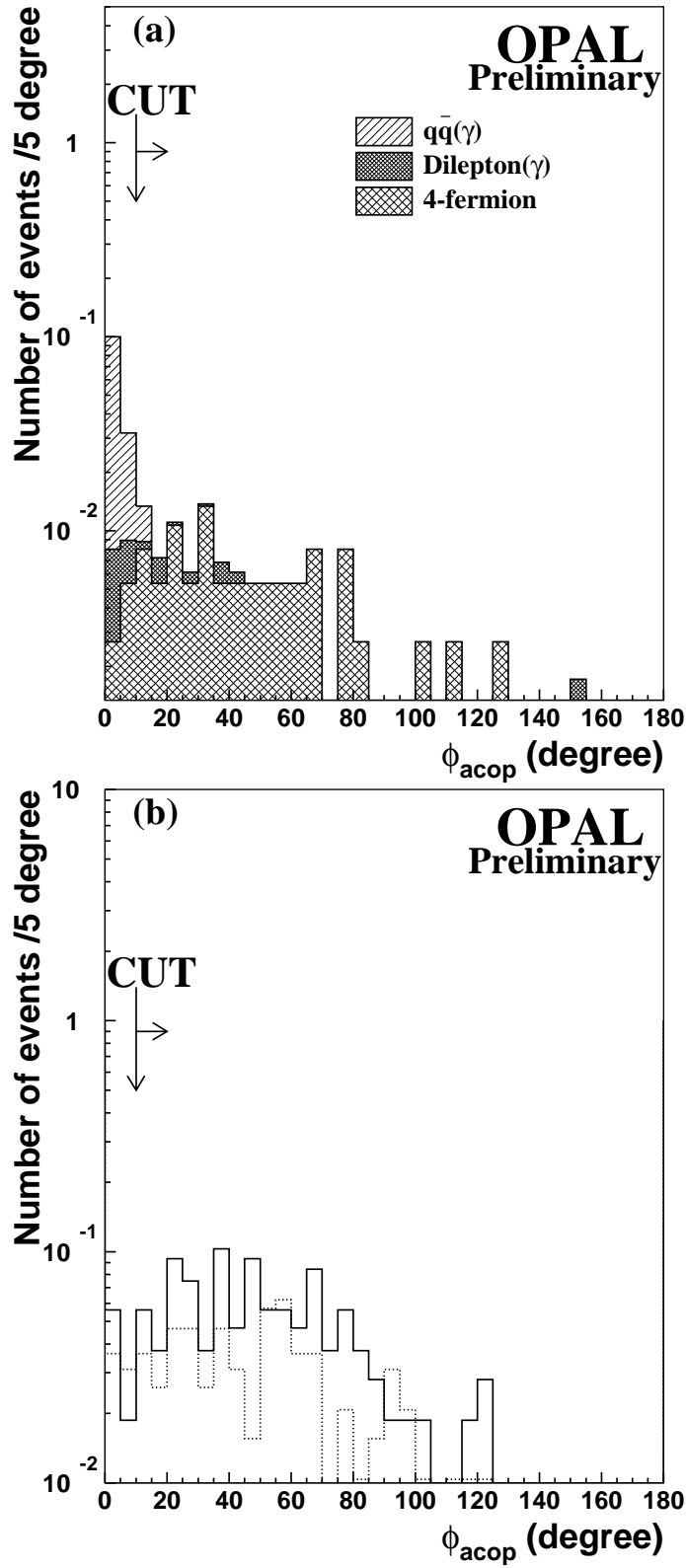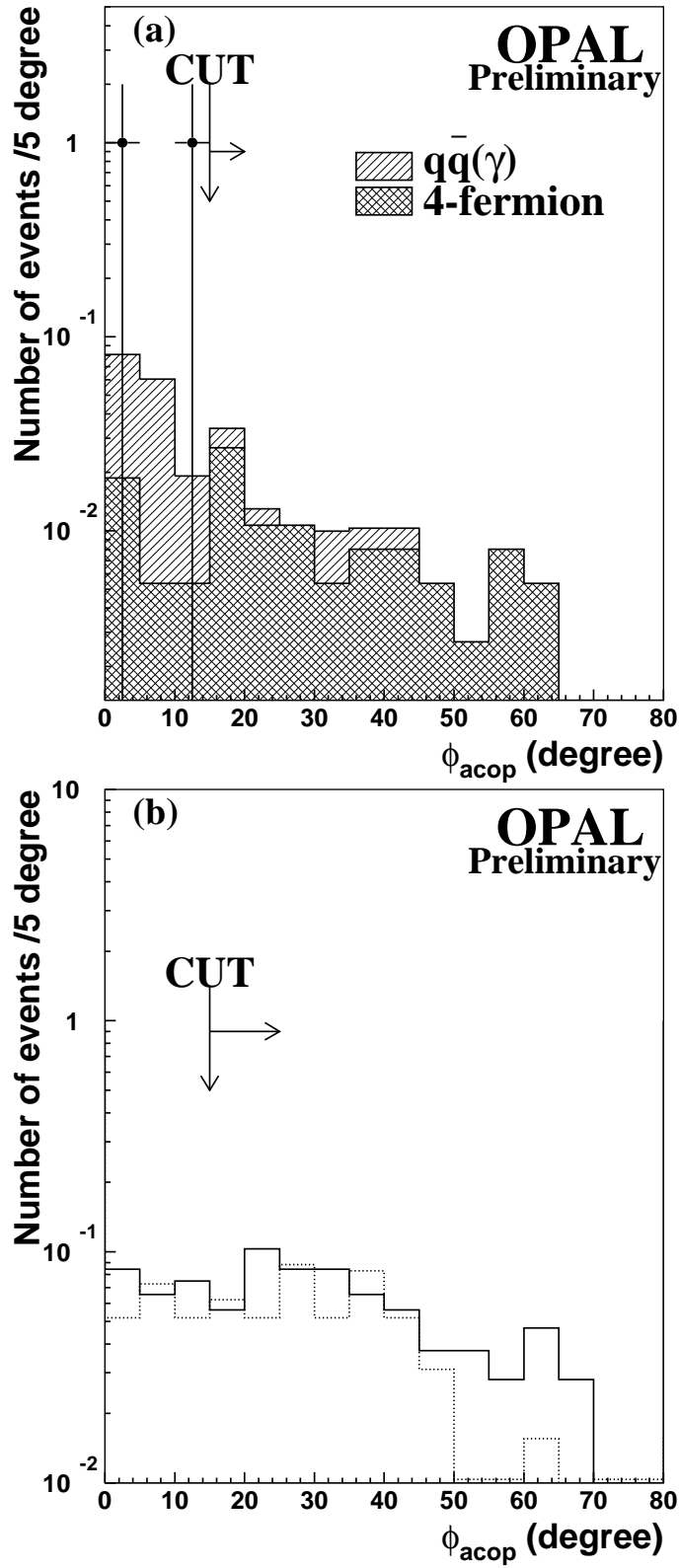
Figure 14: Acoplanarity angle distributions after cut (HL7) for the $L^- \rightarrow \nu_\ell W^{*-}$ case. The convention for indicating the expected signal sample in (b) are the same as in Fig. 13.

27
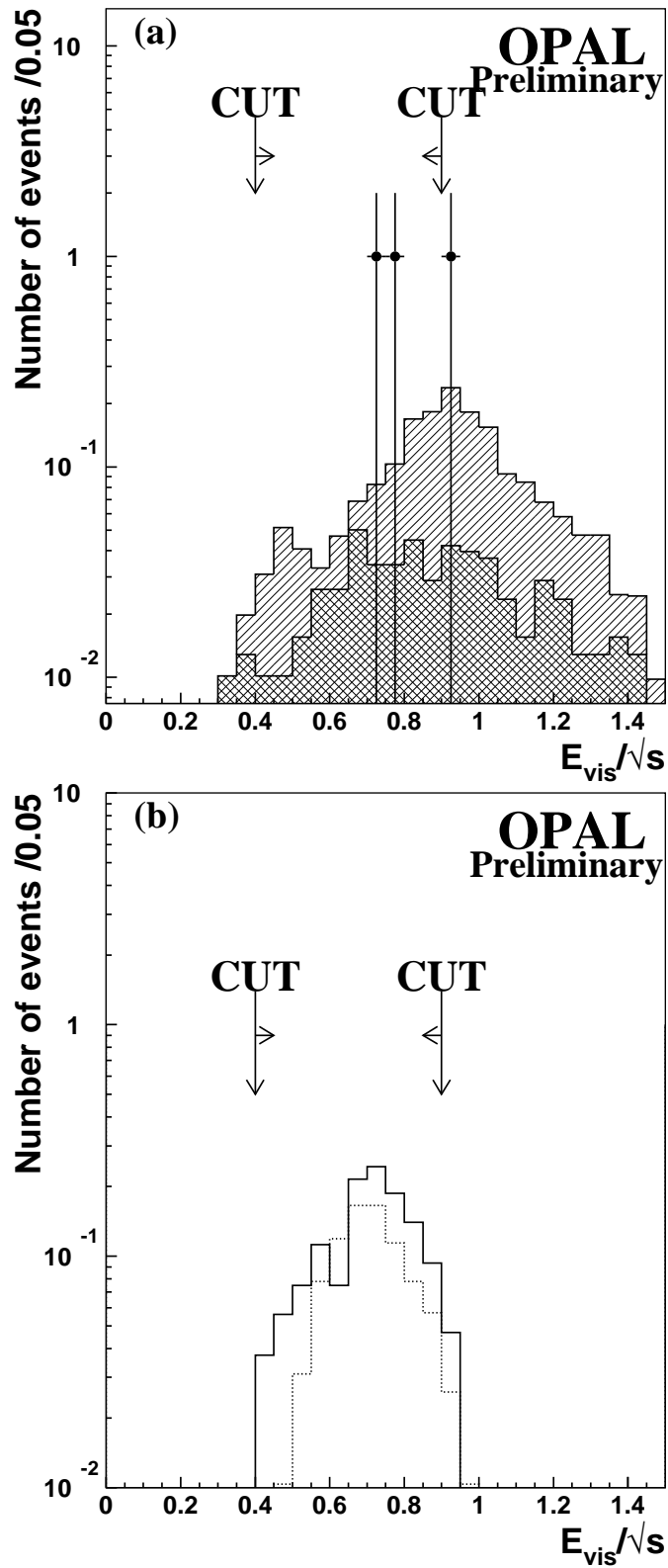
Figure 15: Visible energy distributions for (HH) events normalised to $\sqrt{s}$ after cut (C6). The convention for indicating the background sources in (a) and the expected signal sample in (b) are the same as in Fig. 13.

28

Figure 16: Distributions of E_{back} after cut (HH9) for the $L^- \rightarrow \nu_L W^{*-}$ case. The convention for indicating the expected signal sample in (b) is the same as in Fig. 13.
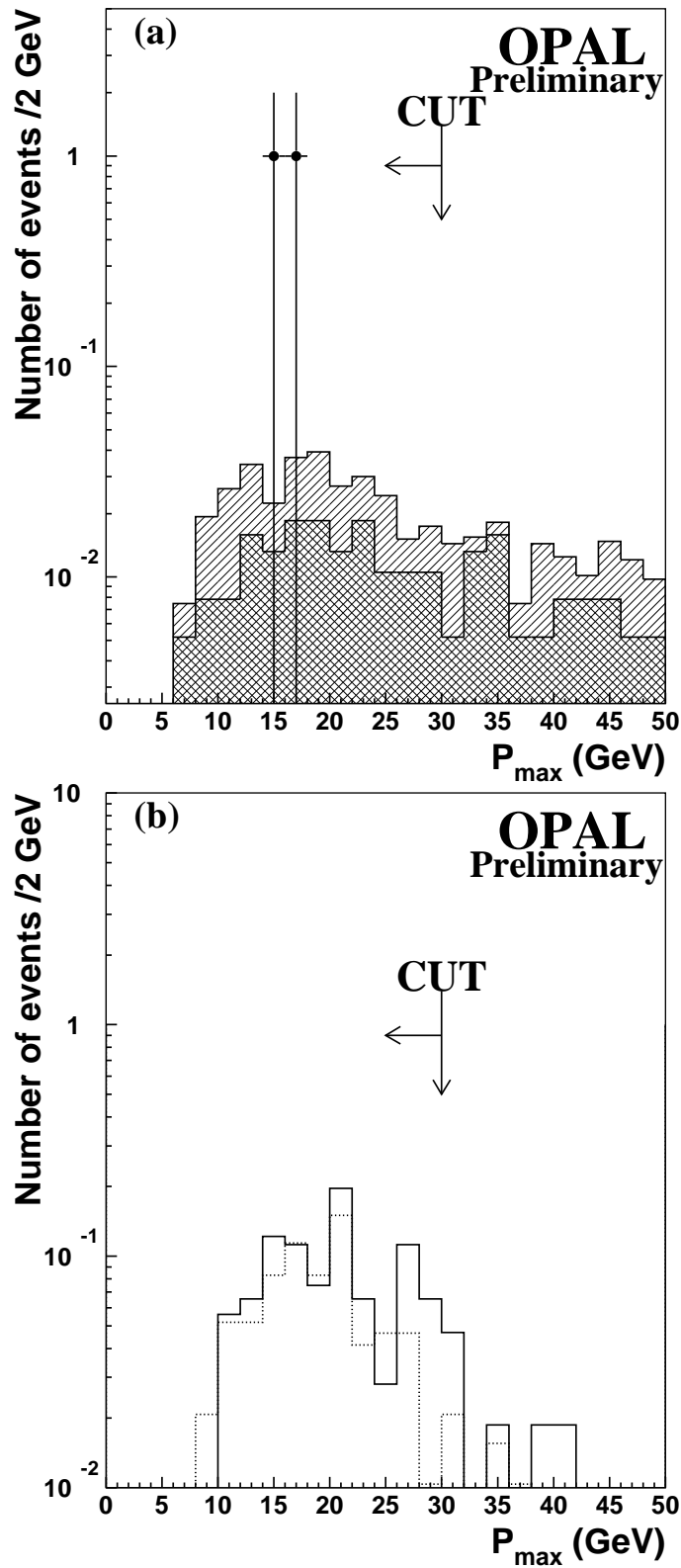
Figure 17: Distributions of the maximum charged track momentum after cut (HH10). The convention for indicating the background sources in (a) and the expected signal sample in (b) are the same as in Fig. 13.

Figure 18: Acoplanarity angle distributions after cut (HH11) for the $L^- \rightarrow \nu_\ell W^{*-}$ case. The convention for indicating the expected signal sample in (b) are the same as in Fig. 13.
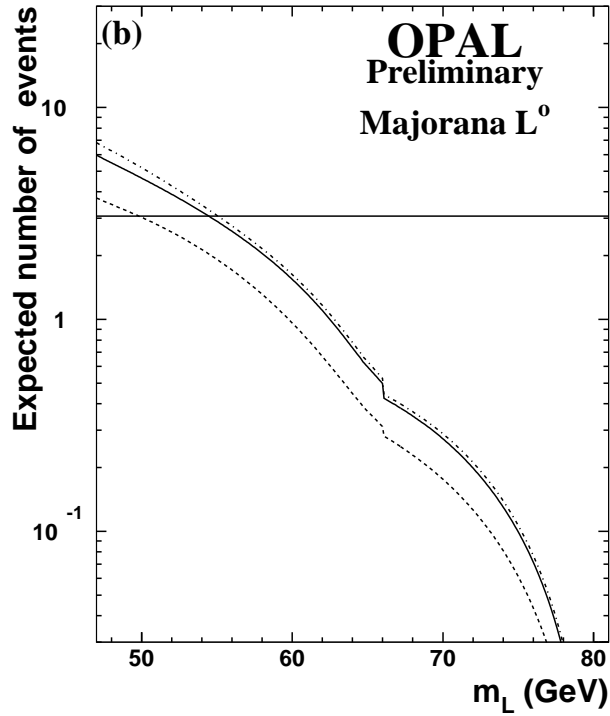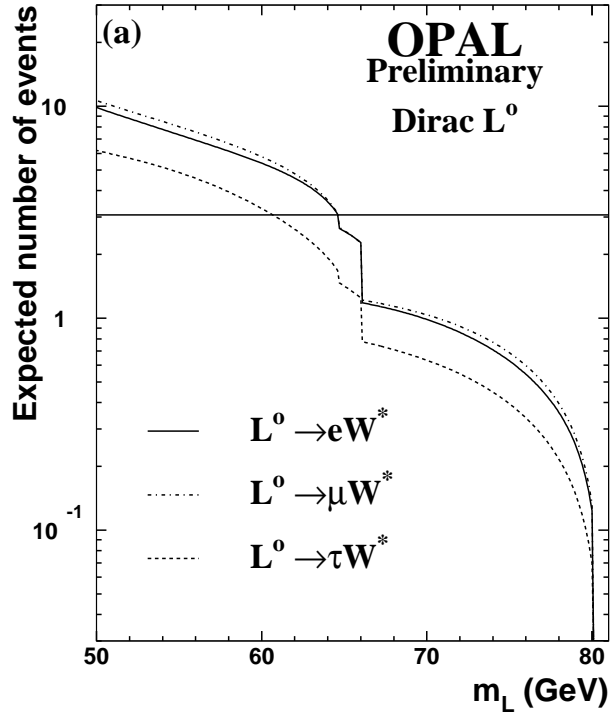
Figure 19: Expected numbers of events as a function of m_{L^0} for $L^0\bar{L}^0 \rightarrow eW^*eW^*$, $\mu W^*\mu W^*$ and $\tau W^*\tau W^*$, respectively, in the Dirac neutral heavy lepton case (a) and the Majorana neutral heavy lepton case (b). The horizontal lines show the threshold number of expected L^0 events at the 95% C.L. limit including systematic errors.
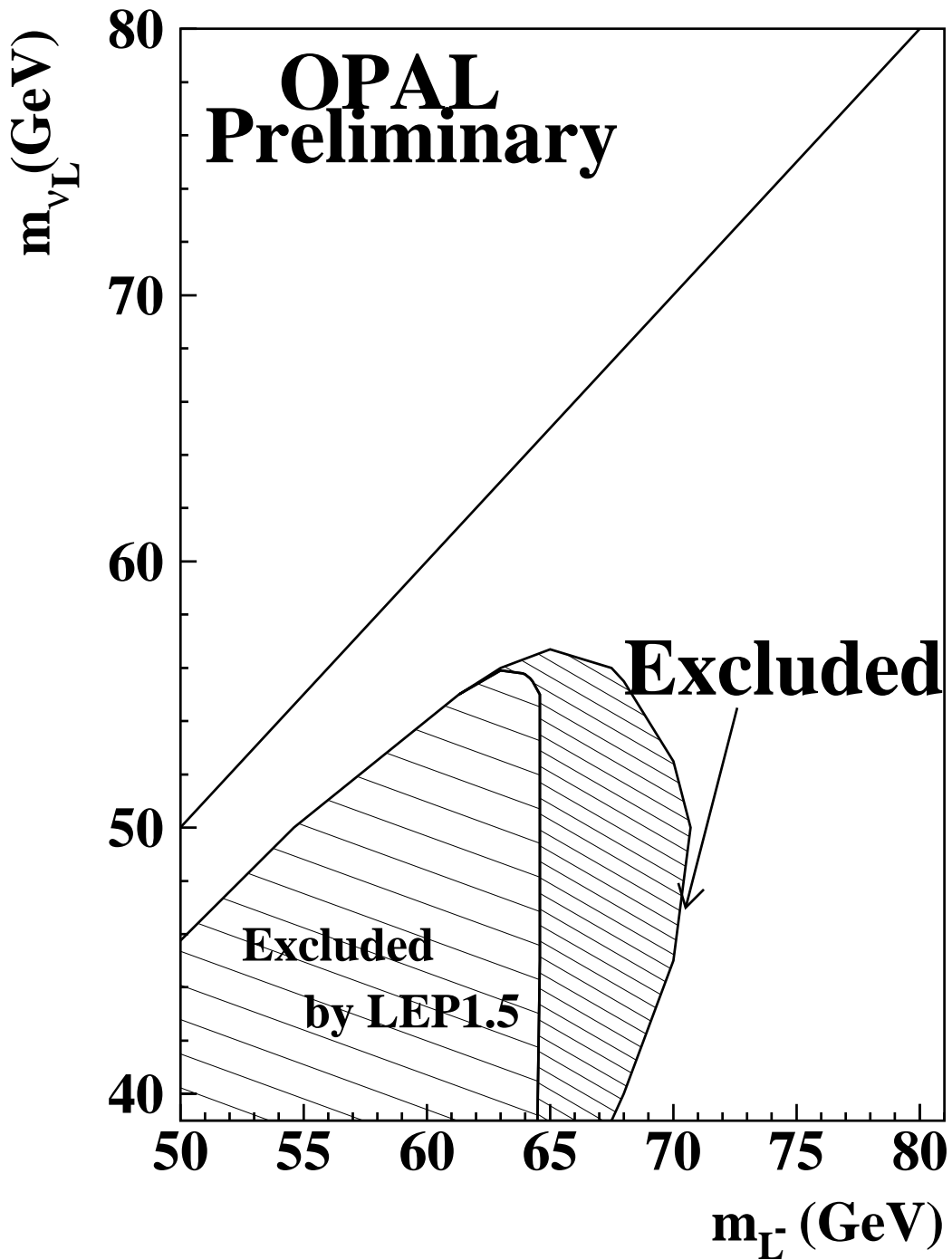
Figure 20: The excluded region in this analysis in the (m_{L^-}, m_{ν_L}) plane for case (B). If L^- decays into $\nu_L + W^{*-}$ and ν_L is assumed to be a stable heavy neutrino, the hatched region is excluded with more than 95% C.L. The region $m_{\nu_L} < 45$ GeV is already excluded for the Dirac ν_L and $m_{\nu_L} < 39.5$ GeV for the Majorana ν_L from the upper limit of the Z^0 decay width measurements at LEP [3]. The diagonal line shows $m_{L^-} = m_{\nu_L}$.
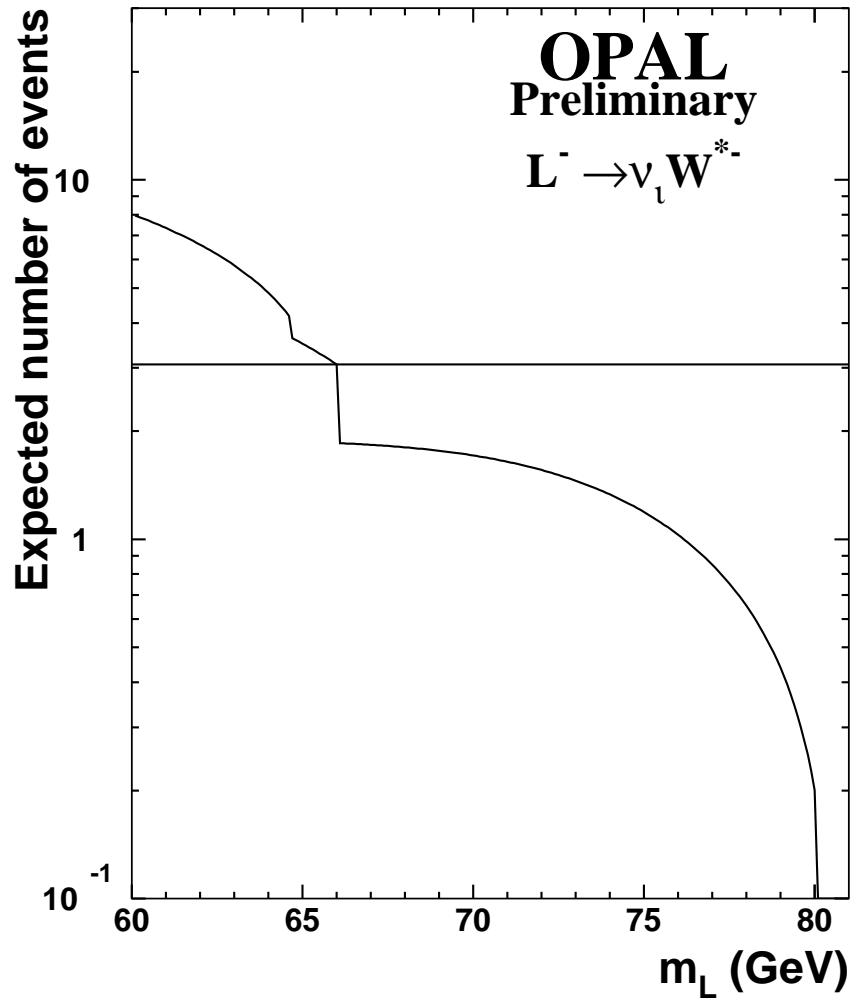
Figure 21: Expected number of events as a function of m_{L^-} for $L^+L^- \rightarrow \nu_\ell W^* \nu_\ell W^*$. The horizontal lines show the threshold number of expected L^- events at the 95% C.L. limit including systematic errors.